nature communications

Article

https://doi.org/10.1038/s41467-026-73119-8

Induced pluripotent stem cell–derived models of malignant nerve sheath tumor progression mimic glial to neuro-mesenchymal transition and uncover therapeutic opportunities

Received: 29 August 2025

Accepted: 4 May 2026

Published online: 17 June 2026

Check for updates

A list of authors and their affiliations appears at the end of the paper

Neurofibromatosis Type 1 (NF1) predisposes to peripheral nerve tumor development. The progression from a benign plexiform neurofibroma (PNF) towards a deadly malignant peripheral nerve sheath tumor (MPNST) is not completely understood but commonly involves the sequential loss of *NF1*, *CDKN2A*, and polycomb repressive complex 2 (PRC2). Here we use an iPSC-derived neural crest (NC) model to reproduce this malignant transformation through gene editing. *NF1-CDKN2A* double-knockout (2KO) NCs form neurofibroma-like tumors in vivo, requiring inactivation of p14ARF and p16INK4a. Additional PRC2 loss (3KO) disrupts pluripotency and induces mesenchymal stem cell-like features. 3KO NCs undergo global chromatin reorganization that prevents gliogenesis by *SOX10* silencing and activates neuro-mesenchymal transcriptional programs recapitulating PNF-ANNUBP-MPNST progression. Upon nerve engraftment, 3KO NC spheres form MPNST-like tumors in vivo, mimicking an early-stage MPNST. Furthermore, we use the 3D NC spheroid models to discover drugs targeting MPNSTs through high-throughput screening of epigenetic compounds. Poly(ADP-ribose) polymerase inhibitors (PARPi) exhibit selective efficacy in PRC2-deficient NC spheroids and Olaparib-Selumetinib combination is well tolerated and significantly suppresses tumor growth in a human MPNST PDX mouse model.

Malignant peripheral nerve sheath tumors (MPNSTs) are aggressive soft tissue sarcomas arising from peripheral nerve cells. Nearly half of all cases are associated with Neurofibromatosis type 1 (NF1), a hereditary cancer syndrome that predisposes to the development of benign and malignant tumors[1]. MPNSTs account for 3–10% of all soft tissue sarcomas, and NF1 patients face a 10–15% lifetime risk of developing them, making MPNSTs the leading cause of mortality in this collective[2,3]. The 5-year survival rate is poor, particularly in the NF1 context[2,4]. No effective therapies exist besides a timely surgery[5].

In NF1, MPNST normally develops through an initial loss of several tumor suppressor genes (TSGs) in a stepwise manner[6–8]. Benign plexiform neurofibromas (PNFs) arise in large nerves from neural crest (NC)–derived Schwann cell precursors (SCP) after *NF1* inactivation[9]. The additional loss of the complete *CDKN2A* locus characterizes the formation of a distinct pre-malignant nodular lesion termed atypical

e-mail: bgel@igtp.cat; marc.ferrer@nih.gov; mcarriol@igtp.cat; eserra@igtp.cat

neurofibromatous neoplasm of uncertain biological potential (ANNUBP)[10,11]. Both lesions share a predominant glial component. The progression toward MPNST involves the loss of polycomb repressive complex 2 (PRC2), a chromatin remodeler complex driving transcriptional repression during development[12], through inactivation of its components *SUZ12* or *EED*[8,13]. This transition is concurrent with a shift toward a mesenchymal identity of tumor cells. *TP53* is also frequently inactivated in MPNSTs, but to a lesser extent[8,14]. After TSG loss, MPNSTs undertake an extensive genomic reorganization, including copy-number alterations and structural variants.

Several in vitro and in vivo models have been developed for PNF, ANNUBP and MPNST, associated with NF1, to study their biology and identify potential new therapies. However, only a few models mimic the progression from benign to malignant NF1 tumors[15–17]. High-throughput screening (HTS) platforms provide a powerful framework to evaluate drug responses, both individually and in combination. Previous HTS efforts in NF1-associated tumors have predominantly relied on two-dimensional (2D) culture models, including immortalized primary PNF-derived Schwann cells (SCs)[18,19] and MPNST cell lines[20].

In this work, we established a human iPSC-derived NC-based model platform with the sequential inactivation of *NF1*, *CDKN2A*, and *SUZ12* to recapitulate the genetic events underlying PNF-MPNST progression. The resulting models captured the glial-to-mesenchymal transition characteristic of neurofibroma-to-MPNST transformation and triple-knockout NC spheroids formed early-stage MPNSTs upon nerve engraftment. Leveraging this platform, we performed an HTS of an epigenetics compound library, identifying PARP inhibitors as selectively active in PRC2-deficient models. Moreover, the PARPi-MEKi combination significantly suppressed tumor growth in a patient-derived MPNST xenograft model. Together, this 3D NC model platform provides a tractable system to study MPNST biology and discover treatment possibilities.

Results

In vivo neurofibroma-like tumor formation of *NF1*(-/-) *CDKN2A*(-/-) neurofibromaspheres requires the loss of p14ARF

We first targeted *CDKN2A* in an *NF1*-deficient iPSC line (1KO_D12) using CRISPR-Cas9[21]. Since *CDKN2A* encodes both p14ARF (p14) and p16INK4a (p16) via alternative reading frames, we designed sgRNAs targeting exon 2: one selectively disrupting p16, and another inactivating both p14 and p16 (Fig. 1A), the latter found in MPNSTs. For practical limitations, we did not generate both single inactivation but only the one selectively disrupting p16 (Fig. 1A) to further explore the role linked to cell cycle alteration and senescence. We successfully generated two *NF1*(-/-) *CDKN2A* p16(-/-) (2KO (p16)), and three *NF1*(-/-) *CDKN2A* p14p16(-/-) (2KO (p14p16)), iPSC lines (Supplementary Fig. 1A, B, Supplementary Data 1). Clonal generation and expansion with p16 inactivated and p14 wild-type (WT) was less efficient than with both proteins inactivated, and one of the 2KO (p16) iPSC lines (2KO_A11) showed abnormal phenotype, slow proliferation, and loss of pluripotency. We confirmed both newly CRISPR-generated mutations at *CDKN2A* and previous *NF1* pathogenic variants, by Sanger sequencing (Supplementary Fig. 1B, Supplementary Data 1). Loss of neurofibromin expression was further validated by western blotting at the iPSC stage (Supplementary Fig. 1C). iPSC lines were characterized by pluripotency marker expression (OCT3/4) and their ability to differentiate into homogeneous populations of NC cells, as assessed by cytometry analysis (p75 and Hnk1) and immunocytochemistry (TFAP2 and SOX10) (Fig. 1B). We further assessed the expression of *CDKN2A* gene products at the protein level. Loss of p16 expression was confirmed at the NC stage by western blotting and immunocytochemistry in both 2KO_C4 (p16-edited) and 2KO_F9 (p14/p16 edited) lines (Supplementary Fig. 1D, E). However, p14 was not expressed in iPSCs nor in NCs, so we differentiated NCs into mesenchymal stem cells (MSCs) and, after several passages, assessed p14 expression by immunocytochemistry. p14 expression was detected in 2KO_C4 (p16-edited) cells but not in 2KO_F9 (p14/p16 edited) (Supplementary Fig. 1F), confirming their genotype status. We performed proliferation and ploidy assays at the NC stage, but no differences were observed compared to the parental 1KO cell line, only deficient in *NF1* (Supplementary Fig. 1G, H). Whole-genome sequencing (WGS) confirmed an isogenic diploid (2n) genome without structural or any other relevant alterations of the 2KO_F9 (p14p16) cell line used for subsequent analysis (Supplementary Fig. 1I).

We then tested the tumor formation capacity of 2KO (p16) and 2KO (p14p16) cell lines. We generated neurofibromaspheres by differentiating NCs toward cells of the SC lineage, and mixed them with primary neurofibroma fibroblasts, allowing them to form spheres for up to 14 days (Fig. 1C, D)[22]. Spheres were engrafted into the sciatic nerve of nude mice and analyzed after 4 months. Tumors developed in 10/15 injections with the 1KO line and in 9/15 with 2KO (p14p16). H&E and S100B staining confirmed neurofibroma-like morphology in both genotypes without evident histological differences. Ku80 staining confirmed the human origin of S100B positive cells (Fig. 1E). In contrast, 2KO (p16) spheres displayed markedly reduced tumorigenicity, with outgrowths in only 3/15 injections that were significantly smaller than those from 1KO or 2KO (p14p16). These findings indicate that, in our model, WT p14 in 2KO (p16) cells impairs proper neurofibroma formation.

2KO NC are sensitive to thymidylate synthase inhibition

Next, we interrogated the impact of *CDKN2A* loss on overall gene expression. We performed RNA-seq of biological triplicates of 1KO and 2KO (p14p16) at iPSC and NC stage, and performed a principal component analysis (PCA) of the global expression (Fig. 1F). p14 and p16 loss had a clear impact on gene expression. We identified several differentially overexpressed genes in 2KO cells compared to 1KO, shared by iPSCs and NCs. Using our own RNA-seq data from tumors developed in NF1 patients, we also identified many differentially overexpressed genes in ANNUBPs compared to PNFs (Fig. 1G). Given the differences in cellular identity between the generated cell lines and tumor cells, and the lower proportion of 2KO cells in ANNUBPs compared with the proportion of 1KO cells in PNFs[7], we identified only three genes that were commonly overexpressed in both 2KO cells and ANNUBPs. One of them was *TYMS*, encoding for thymidylate synthase (TS) (Fig. 1H). The described synthetic lethality between loss of *CDKN2A* and TS inhibition[23] prompted us to test the sensitivity of 2KO NC cells to TS inhibitors compared to 1KO NCs. We used the TS inhibitor Pemetrexed on 1KO and 2KO NC cultures (Fig. 1I–K) and observed a higher sensitivity of 2KO NCs to *TYMS* inhibition (Fig. 1I, J). We also observed marked morphological changes in the cells, including increased size, aberrant nuclei, and enlarged cytoplasm in 2KO cells (Fig. 1K).

Inactivation of *NF1*, *CDKN2A* and PRC2 in iPSCs exhibits a biologically imposed order

Next step involved the inactivation of PRC2, through targeted editing of *SUZ12*, in 1KO, 2KO (p16) and 2KO (p14p16) iPSCs. We were able to assess PRC2 functional loss by directly interrogating the absence of the trimethylation of lysine 27 of histone 3 (H3K27me3), using a specific antibody (Fig. 2A). We performed multiple transfections in each cell line (Fig. 2B) successfully achieving *SUZ12* editing in three genotypically distinct iPSCs (Fig. 2C). However, when trying to perpetuate the different edited clones, we did not succeed for 1KO and 2KO (p16), that is, for those iPSCs with preserved p14ARF function (Supplementary Fig. 2A, B). However, we were able to establish clones from 2KO (p14p16) edited iPSCs and perpetuate them at the NC stage (see below), obtaining 3KO cell lines with no functional *NF1*, *CDKN2A* (p14p16) and *SUZ12* (Fig. 2B, D). These results suggested the possibility that the order of TSG inactivation in *NF1*(-/-) iPSCs required a

https://doi.org/10.1038/s41467-026-73119-8

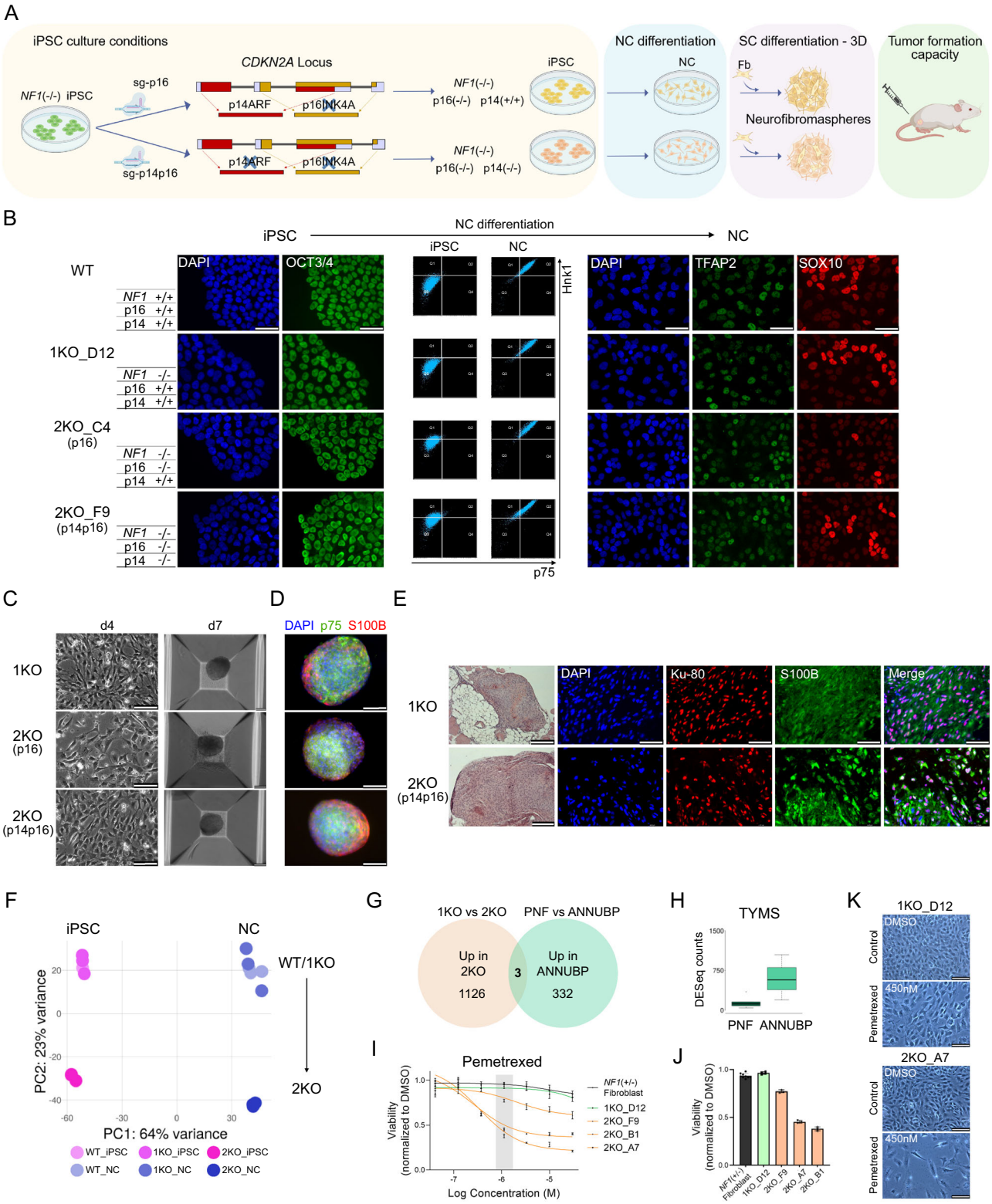

biologically imposed specific sequence: first, the complete inactivation of the *CDKN2A* locus (involving p14 and p16) and then the loss of PRC2.

To support these findings, we tested doxycycline-inducible re-expression of p14 or p16 in 2KO (p14p16) and 3KO NC cells using lentiviral bicistronic vectors co-expressing p14-GFP or p16-mCherry (Fig. 2E). Fluorescence was quantified at baseline (24 h) and after 5 and 8 days post-initial induction. Expression was also induced 24 h before day 5 and 8 in independent cultures and measured on these days, to control for lentiviral silencing (Fig. 2F). Fluorescent cell percentages differed between 2KO and 3KO lines (Fig. 2G), consistent with variable lentiviral silencing. In 2KO (p14p16) NC cells, p14 re-expression did not affect viability, whereas p16 re-expression markedly reduced survival (Fig. 2Gi, ii). In 3KO cells, re-expression of either p16 or particularly p14 severely compromised viability (Fig. 2Giii, iv), aligning with the inability to expand PRC2-edited 3KO lines from 2KO (p16). Altogether, these results suggest that in the context of PNF-ANNUBP-MPNST progression, cells with no functional *NF1* are not viable after losing PRC2, if either of the two genes encoded by *CDKN2A* remains

Fig. 1 | Generation of double knockout *NF1*(-/-) *CDKN2A*(-/-) iPSC lines. **A** Schematic representation of the editing strategy used to knock out the *CDKN2A* locus in *NF1*(-/-) iPSCs, followed by neural crest (NC) formation and Schwann cell (SC) differentiation to generate neurofibromaspheres and assess tumorigenic potential. Sg: sgRNA; Fb: PNF-derived fibroblast. Created in BioRender. Carrió, M. (2026) https://BioRender.com/u74buvi. **B** Left panel: OCT3/4 expression in iPSCs: wild type WT (*NF1*+/+); 1KO (*NF1* -/-); 2KOp16 (*NF1* -/- *CDKN2A* p16INK4a -/-); and 2KOp14p16 (*NF1* -/- *CDKN2A* -/-). Middle panel: Flow cytometry analysis of p75 and Hnk1 before (iPSC) and after NC differentiation ($n = 2$ independent experiments). Right panel: TFAP2 and SOX10 expression at NC stage. Scale bar: 50 μm. **C** Left: Micrographs of NC cells after 4 days (d4) of SC differentiation. Scale bar: 100 μm. Right: representative neurofibromaspheres at day 7 (d7) of SC differentiation, containing also PNF-derived fibroblasts ($n = 3$ independent experiments). Scale bar: 100 μm. **D** Representative immunofluorescence images showing p75 (green) and S100B (red) expression in neurofibromaspheres. Scale bar: 100 μm. **E** Characterization of the tumors grown after engraftment of neurofibromaspheres in the sciatic nerve of nude mice. Left panel: H&E staining. Scale bar: 200 μm. Right panel: Immunofluorescence images for Ku-80 and S100B. Scale bar: 50 μm ($n = 15$ tumors per model analyzed). **F** Principal component analysis (PCA) of global gene expression of WT, 1KO and 2KO cell lines at iPSC and NC stage. One WT in triplicate and three 1KO and 2KO cell lines are shown. **G** Schematic representation of upregulated genes shared by 2KO NCs and ANNUBPs. **H** *TYMS* expression in PNFs ($n = 6$ independent human tumors) and ANNUBPs ($n = 3$ independent human tumors). Boxplots show the median (center line), upper and lower hinges (box limits), and whiskers extending to the most extreme value within 1.5× the interquartile range from the hinges; points beyond the whiskers are shown individually as outliers. **I** Cell viability dose-response curves for Pemetrexed treatment after 96 h in 1KO_D12 NC, 2KO NC, and *NF1*(+/−) fibroblast cell line, assessed by CellTiter-Glo assay. Mean ± SD of technical replicates ($n \geq 3$), from 3 biological 2KO cell lines. **J** Cell viability after 1.11 μM pemetrexed treatment in cell lines from (**I**). Mean ± SD of technical replicates ($n \geq 3$). **K** Representative micrographs showing density and morphology changes between 1KO_D12 NC and 2KO_A7 NC cell lines after 96 h of 450 nM pemetrexed treatment ($n = 3$ independent experiments). Scale bar: 100 μm. Source data are provided as a Source Data file.

functional, consistent with the observed complete inactivation status of the *CDKN2A* locus in MPNSTs[24].

PRC2 loss in *NF1*(-/-) *CDKN2A*(-/-) iPSCs induces loss of pluripotency, mesenchymal identity acquisition, and can be perpetuated as neural crest

Inactivation of *SUZ12* in 2KO (p14p16) iPSCs resulted in clones that, under iPSC conditions, underwent spontaneous differentiation and progressively acquired a mesenchymal-like phenotype, eventually leading to proliferative arrest and senescence (Fig. 3A–C). Flow cytometry revealed expression of mesenchymal stem cell (MSC) markers (CD73, CD13, and CD44) consistent with a shift toward a MSC-like identity (Fig. 3D). Immunostaining confirmed OCT3/4 downregulation and SOX9 upregulation in 3KO cells compared to 2KO iPSCs (Fig. 3E). 3KO cells were non-viable under standard iPSC culture conditions; nevertheless, we were able to perpetuate them under NC culture conditions and establish three independent non-perishable 3KO cell lines (Fig. 3F, G, Supplementary Fig. 3A, B, Supplementary Data 1). Flow cytometry confirmed expression of NC markers HNK1 and p75 (Fig. 3H). However, 3KO NCs also displayed elevated levels of MSC markers compared to their 1KO and 2KO counterparts (Fig. 3H, Supplementary Fig. 3C). Proliferation rates and ploidy of 3KO NCs remained basically unchanged compared to 1KO and 2KO (Supplementary Fig. 3D, E). All 3KO NC cell lines also exhibited an unaltered 2n genome assessed by WGS analysis (Supplementary Fig. 3F). Notably, immunofluorescence for SOX10 and SOX9—key NC transcription factors (TFs)—revealed an inverse relationship across 1KO, 2KO, and 3KO NCs: while SOX10 expression gradually diminished and was absent in 3KO NCs, SOX9 reached a maximum protein expression in these cells (Fig. 3I, Supplementary Fig. 3G). Moreover, 3KO NCs exhibited a drastic downregulation of glial genes (*SOX10*, *NGFR*, *PLP1*), and an upregulation of mesenchymal markers (*SOX9*, *TWIST1*, *PRRX1*) (Fig. 3J) compared to 2KO NCs, as assessed by bulk-RNAseq analysis, suggesting a glial-to-mesenchymal shift.

3KO NC spheroids generate human MPNST-like tumors upon nerve engraftment in nude mice

To functionally test these identity changes and the potential of 3KO NCs to form tumors in vivo, we performed a tumor formation assay by engrafting 3KO NC-like spheroids in contact with the sciatic nerve of nude mice, together with 1KO and 2KO neurofibromaspheres for comparative purposes. After 4 months, mice were sacrificed. We identified large, highly nucleated human tumors at the injection site of the 3KO NC-like spheroids, adjacent to the nerve (Fig. 4A). These tumors exhibited numerous mitotic figures and a histology compatible with an MPNST by H&E staining, as assessed by an expert NF1 pathologist. We confirmed the human origin of these cells by Ku-80 staining (Fig. 4A). Neurofibromaspheres derived from 1KO and 2KO NCs generated neurofibroma-like tumors as previously described[21] (Figs. 1E, 4B). Immunostaining for H3K27me3, SOX10, S100B, vimentin, and Ki67 was performed (Fig. 4B). 1KO and 2KO tumors retained H3K27me3 and expressed SOX10/S100B, whereas 3KO tumors lacked these markers, confirming PRC2 loss and loss of neurofibroma-like identity. All tumors were Vimentin and Ki67 positive, with slightly higher Ki67 in 3KO tumors, suggesting increased proliferation. These findings demonstrated that 3KO NC spheres can generate early-stage MPNSTs, establishing a relevant model for studying malignant progression and drug testing.

MPNST cell identity is highly impacted by PRC2 inactivation and MSC-like features

3KO NC cells model early MPNST development (TSG inactivation, 2n genome), whereas established MPNST cell lines represent a late stage of disease (TSG inactivation, rearranged genome). To identify molecular features gained during this progression, we compared both in vitro models, focusing the analysis on how PRC2 loss and mesenchymal identity acquisition shape MPNST cell identity (Fig. 5A).

For that, we first differentiated 3KO NC lines and their parental 2KO, 1KO and WT isogenic NC lines into MSCs (Fig. 5B, Supplementary Fig. 4A). Differentiating 3KO NCs into MSCs led to early proliferative arrest and senescence (Supplementary Fig. 4B), preventing the generation of stable 3KO MSC lines. However, sufficient MSCs were obtained to enable multiple downstream analyses. We included all different genotypes and cell identities, from iPSCs to NC and MSCs, and five MPNST cell lines bearing the inactivation of *NF1*, *CDKN2A* and *SUZ12* (Fig. 5B).

We performed transcriptome (RNA-seq) for all cell types; methylome (EPIC array) for NCs, MSCs and MPNST cell lines, and chromatin accessibility analysis (ATAC-seq) for NCs. PCAs evidenced a profound contribution of both PRC2 loss and MSC expression in defining the identity of MPNST cell lines, with a clear impact of both factors on transcriptome and methylome profiles (Fig. 5Ci, ii). In addition, the loss of PRC2 also had a profound effect on chromatin accessibility in NCs, as expected (Fig. 5Ciii). An integrative analysis of these three datasets, comparing 2KO vs 3KO NCs, identified several genes shared across them (Supplementary Fig. 5, Supplementary Data 2), highlighting the significant relationship among chromatin accessibility, methylation status and gene expression.

We also compared the expression of 2KO and 3KO NC lines in a more detailed analysis to assess the impact of PRC2 loss at the NC stage. Differentially expressed genes were visualized in a heatmap alongside MPNST cell lines, NCs and MSC genotypes; these were included for visualization purposes and excluded from the

https://doi.org/10.1038/s41467-026-73119-8

A

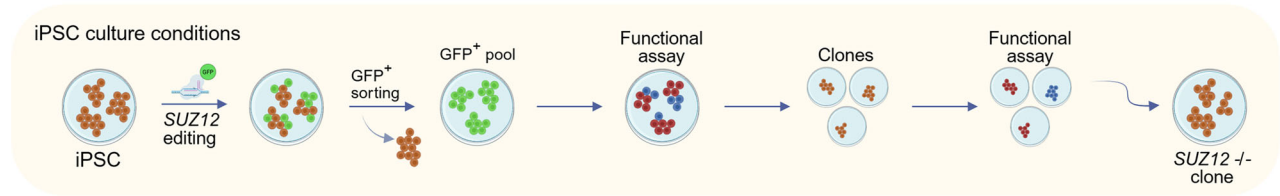

B

Cell lines	Genotype	Transfections	Edited cell pools	Analyzed clones	Edited clones	Expanded clones
1KO	*NF1* (-/-) p14 (+/+) p16 (+/+)	4	2	29	1	0
2KO (p16)	*NF1*(-/-) p14 (+/+) p16 (-/-)	4	4	30	3	0
2KO (p14p16)	*NF1*(-/-) p14 (-/-) p16 (-/-)	5	4	46	8	4

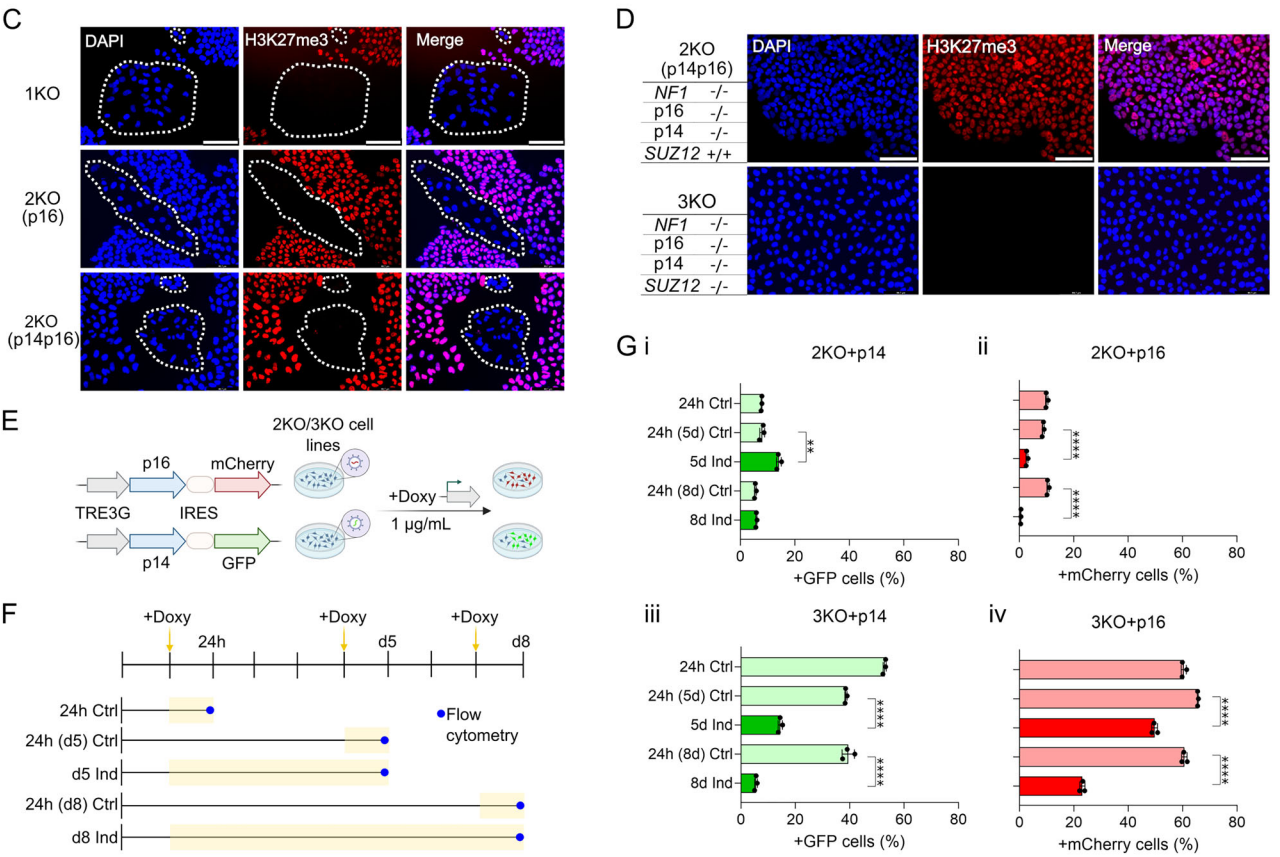

Fig. 2 | A biological constraint for the inactivation of *NF1*, *CDKN2A* and PRC2 in iPSCs. A Schematic representation of the editing strategy used to knock out *SUZ12* in iPSCs and screening workflow for edited clones. Created in BioRender. Carrió, M. (2026) https://BioRender.com/ie3019z. **B** Quantification of editing efficiency and clonal progression at each stage of the *SUZ12* editing workflow. **C** Immunofluorescence detection of H3K27me3 in transfected 1KO and 2KO cell pools. *SUZ12*-edited cells are indicated by white dashed lines ($n \geq 4$ independent experiments). Scale bar: 100 µm. **D** Immunofluorescence of H3K27me3 in 2KO (p14p16) parental line and an expanded 3KO clonal line ($n \geq 4$ independent experiments). Scale bar: 100 µm. **E** Diagram of lentiviral doxycycline-inducible systems for p16 and p14 re-expression in 2KO and 3KO cell lines. Created in BioRender. Carrió, M. (2026) https://BioRender.com/f46q463. **F** Experimental design scheme for the inducible p14 and p16 expression in 2KO and 3KO cells. Transduced cells were treated with doxycycline either at day 5 (d5) or day 8 (d8), and expression levels of p16 (mCherry) and p14 (GFP) were assessed by flow cytometry. Control cells were treated with doxycycline for 24 h prior to each measured time point (d1, d5 and d8). **G** Flow cytometry analysis of GFP+ and mCherry+ cell populations at d5 and d8 post-doxycycline induction. (**i**) p14 re-expression in 2KO cell line, (**ii**) p16 re-expression in 2KO cell line, (**iii**) p14 re-expression 3KO cell line, (**iv**) p16 re-expression 3KO cell line. Data represent mean ± SD from three independent experiments. Unpaired two-tailed *t* tests: $^{**}p < 0.01$; $^{****}p < 0.0001$. Exact *p*-values and Source data are provided as a Source Data file.

comparison (Fig. 5D, Supplementary Data 3). Unsupervised clustering separated samples into two groups based on PRC2 status, with a shared set of upregulated genes (Cluster N1) identified in 3KO NCs, 3KO MSCs, and MPNST cell lines. Gene enrichment analysis of cluster N1 revealed strong associations with neurogenesis-related processes (Fig. 5E, Supplementary Fig. 6A, Supplementary Data 3). In addition, we identified cluster G, enriched in genes related to gliogenesis, that was downregulated in 3KO NCs compared to PRC2 WT NCs (Fig. 5F, Supplementary Fig. 7, Supplementary Data 4). We also compared 3KO NCs with established MPNST cell lines to identify features absent in 3KO NCs key to becoming full MPNST cells. MSCs and additional samples were included for visualization purposes and excluded from the comparison. Unsupervised clustering of differentially expressed genes separated cell lines with NC identity from those with a mesenchymal identity (MSCs and MPNST cell lines), regardless of their genotype (Fig. 5G, Supplementary Data 5). We identified a set of genes

https://doi.org/10.1038/s41467-026-73119-8

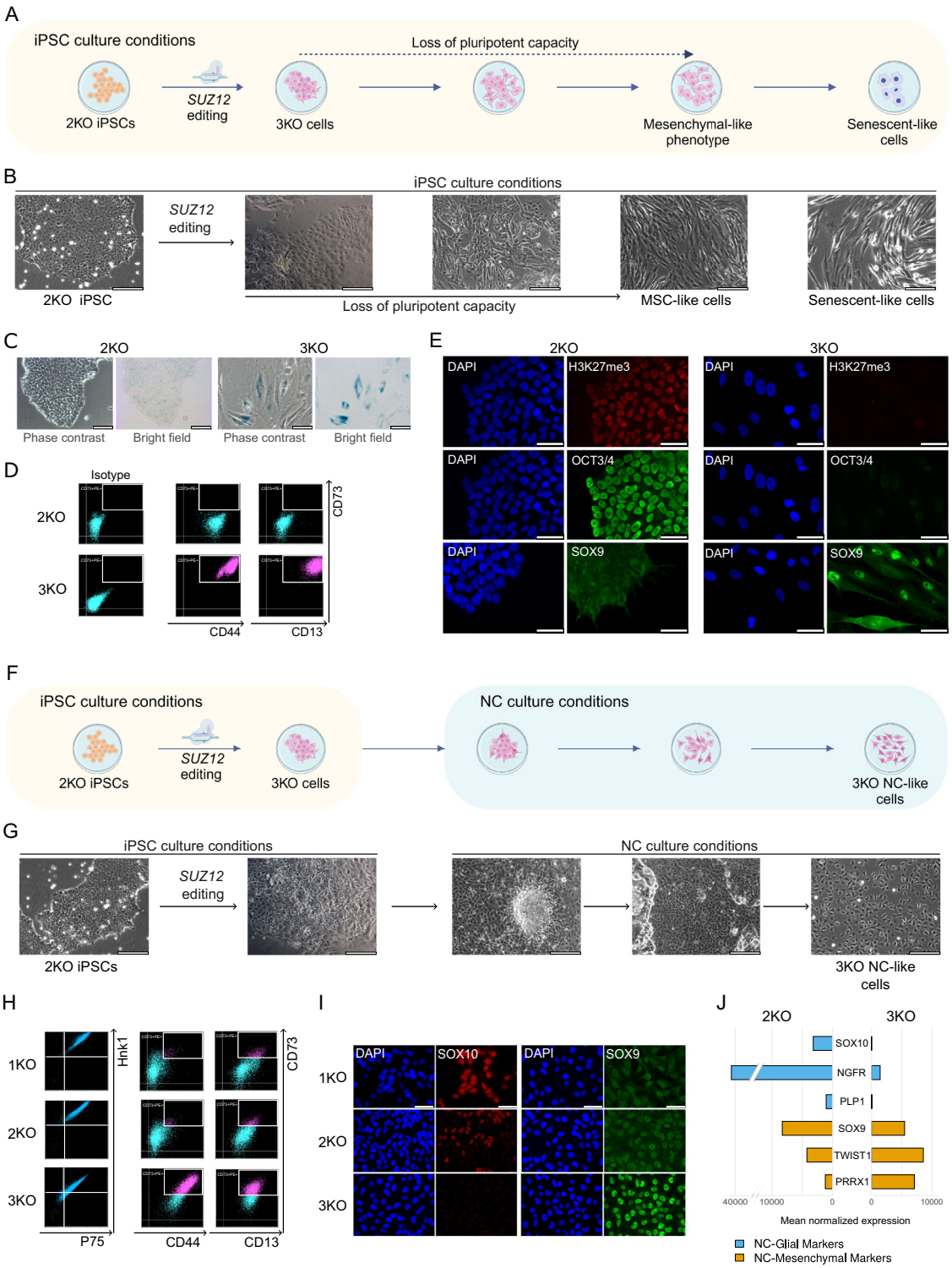

Fig. 3 | Loss of PRC2 function in 2KO iPSCs induces loss of pluripotency and transition toward a mesenchymal-like identity. A Schematic representation of the acquired cell fate of 2KO cells after *SUZ12* editing in iPSC culture conditions. Created in BioRender. Carrió, M. (2026) https://BioRender.com/ru73nnd. **B** Representative micrographs illustrating loss of pluripotency, acquisition of an MSC-like phenotype, and senescence onset in 3KO *SUZ12*-edited cells ($n = 4$ independent clones). Scale bar: 200 μm. **C** Representative micrographs of senescence analysis (X-Gal staining in blue) in 2KO and 3KO cell lines ($n = 3$ independent experiments). Scale bar: 100 μm. **D** Flow cytometry analysis of MSC markers CD13, CD44 and CD73 ($n = 3$ independent experiments). **E** Immunofluorescence images illustrating pluripotency (OCT3/4), PRC2 function (H3K27me3) and mesenchymal identity (SOX9) in 2KO and 3KO cell lines ($n = 2$ independent experiments). Scale bar: 50 μm. **F** Schematic representation of the strategy used to perpetuate 3KO *SUZ12*-edited cells under NC culture conditions. Created in BioRender. Carrió, M. (2026) https://BioRender.com/wbrqpus. **G** Representative micrographs showing NC-like phenotype acquisition of 3KO cells under NC culture conditions ($n = 3$ independent clones). Scale bar: 200 μm. **H** Flow cytometry for NC markers (p75 and Hnk1) and MSC markers (CD13, CD44 and CD73) in 1KO, 2KO and 3KO cell lines ($n = 3$ independent experiments). **I** Immunofluorescence of SOX10 and SOX9 expression in 1KO, 2KO and 3KO cell lines ($n = 2$ independent experiments). Scale bar: 50 μm. **J** Expression of selected NC-glial (*SOX10*, *NGFR*, *PLP1*) and NC-mesenchymal (*SOX9*, *TWIST1*, *PRRX1*) markers in 2KO ($n = 3$ biological replicates) and 3KO ($n = 3$ biological replicates) cell lines.

https://doi.org/10.1038/s41467-026-73119-8

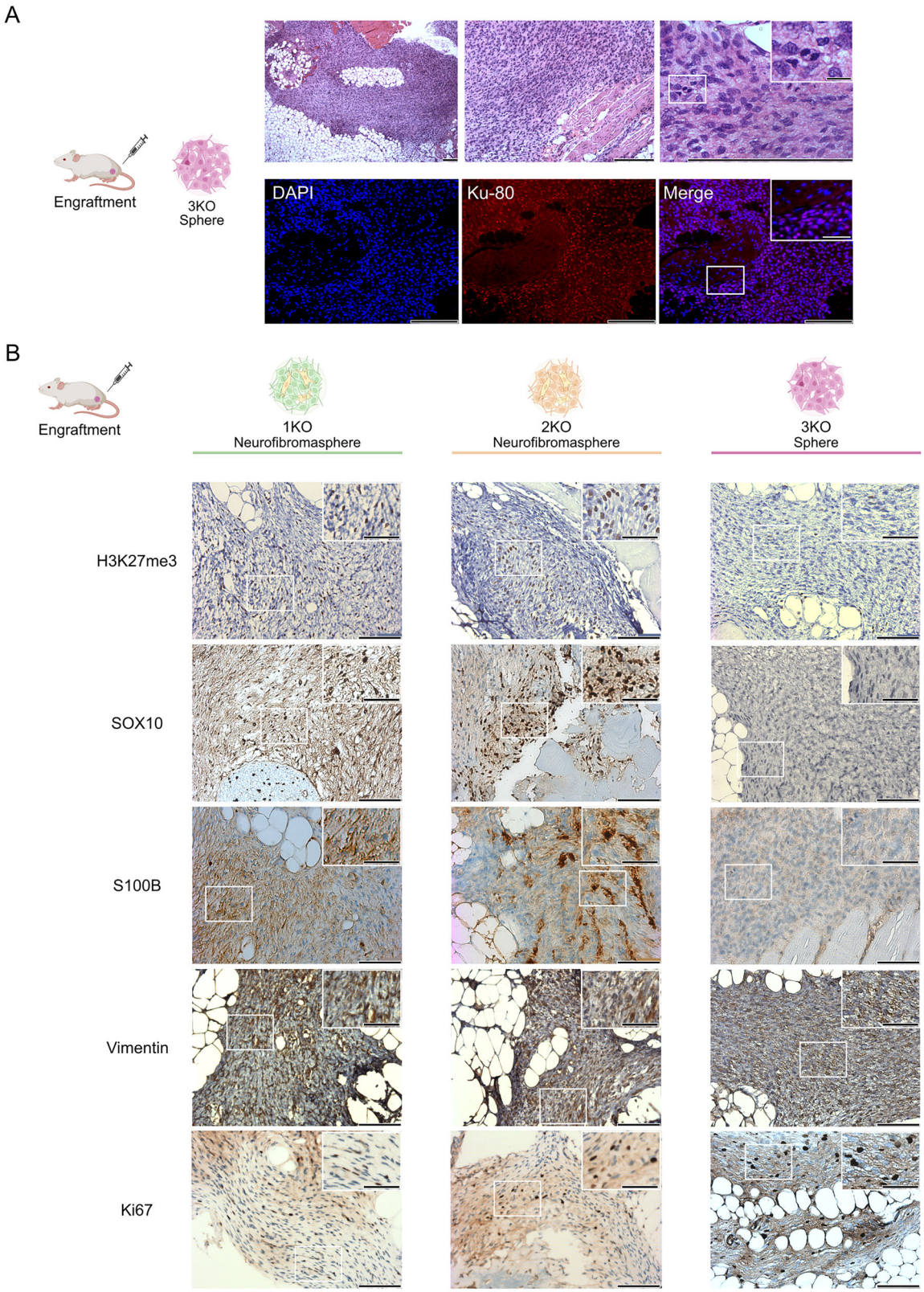

Fig. 4 | 3KO NC spheroids generate human MPNST-like tumors in vivo mimicking early-stage MPNST development. A Characterization of tumors arising from 3KO NC spheroid engraftment into the sciatic nerve of nude mice. Upper panel: representative hematoxylin and eosin (H&E) images showing high cellularity and mitotic activity ($N = 12$ tumors). Scale bar: 200 μm. Lower panel: Ku-80 immunofluorescence with DAPI nuclear counterstaining, showing human origin ($n = 4$ tumors). Scale bar: 200 μm. Higher-magnification images of the same field; black scale bar: 13 μm, white scale bar: 80 μm. Created in BioRender. Carrió, M. (2026) https://BioRender.com/d8zwyze. **B** Immunohistochemical comparison of 1KO, 2KO, and 3KO tumor models showing H3K27me3, SOX10, S100B, Vimentin, and Ki67 expression. Scale bar:100 μm. Higher-magnification image of the same field; scale bar: 50 μm. n = 12 tumors from each model were analyzed. Created in BioRender. Carrió, M. (2026) https://BioRender.com/o8oiz21.

https://doi.org/10.1038/s41467-026-73119-8

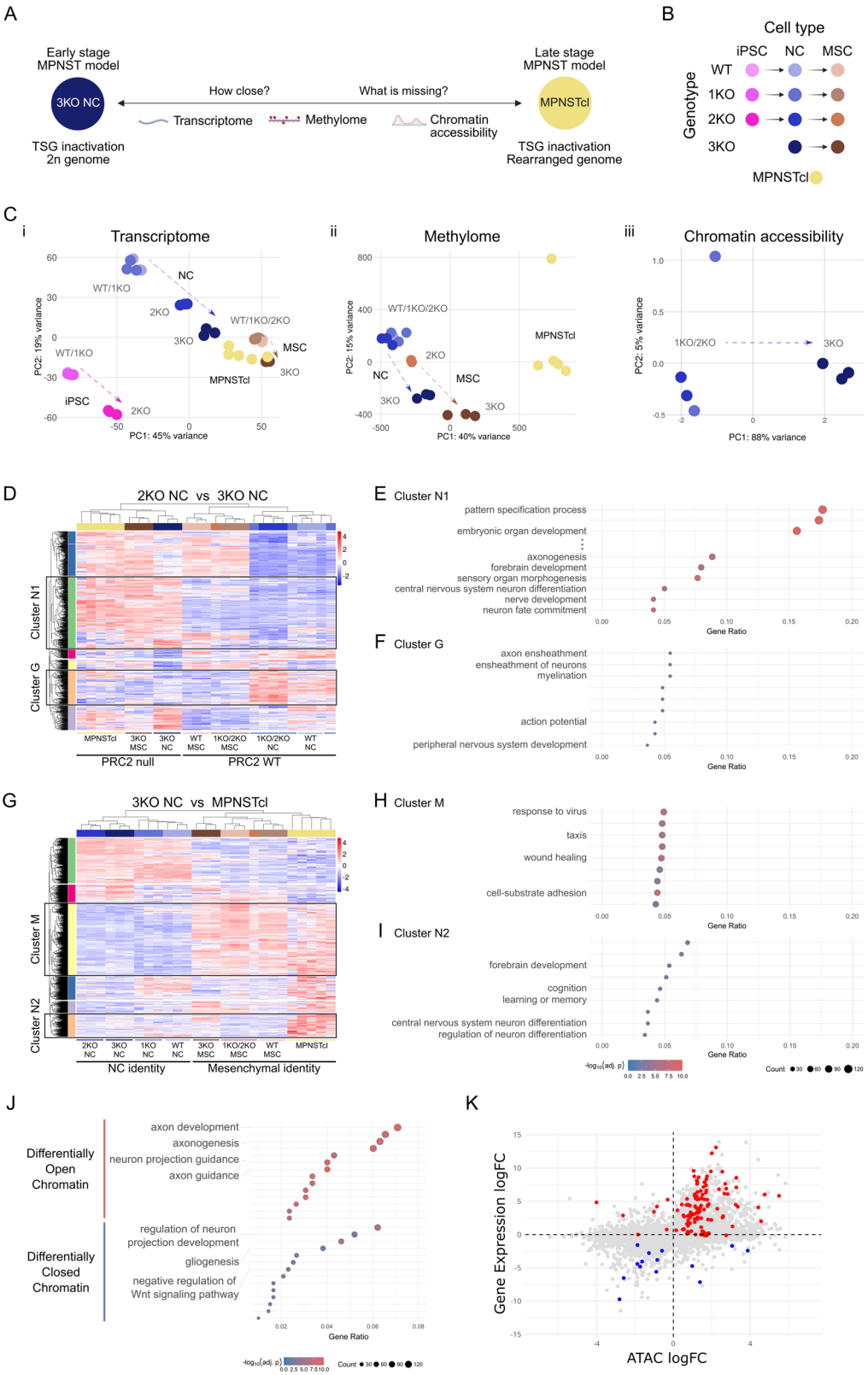

upregulated in cells with mesenchymal identity (Cluster M). Enrichment analysis of cluster M revealed multiple processes associated with mesenchymal identity, including 73 genes involved in wound healing (Fig. 5H, Supplementary Data 5). Furthermore, we identified an additional group of genes upregulated only in MPNST cell lines (Cluster N2). Interestingly, enrichment analysis of this cluster identified biological processes that were also related to neurogenesis (Fig. 5I, Supplementary Fig. 6B, Supplementary Data 5), indicating its importance for MPNST identity.

Global expression analysis highlighted a glial-to-neuro-mesenchymal transition from 2KO to 3KO NC cells, mimicking features of ANNUBP-MPNST progression. To investigate the role of chromatin remodeling in this transition, we analyzed ATAC-seq data. Enrichment analysis of differential chromatin accessibility between

Fig. 5 | MPNST phenotype is markedly affected by PRC2 inactivation, the presence of neurogenesis and MSC-like traits and gliogenesis downregulation. **A** Schematic overview of the transcriptomic and epigenomic comparison between 3KO NC and MPNST cell lines (MPNSTcl) in vitro models. Created in BioRender. Carrió, M. (2026) https://BioRender.com/5mez15q. **B** Schematic representation showing the cell lines used for the omics analyses. **C** Principal component analysis (PCA) of cell types in (**B**), comparing (**i**) transcriptome, (**ii**) methylome and (**iii**) chromatin accessibility. Arrows indicate the impact of genotype on the different cell type identities. Each dot represents a sample. Samples from each group are independent biological replicates. **D** Heatmap showing the expression patterns across all samples of genes differentially expressed between 2KO ($n = 3$ biological replicates) and 3KO NC ($n = 3$ biological replicates). The differentially expressed genes from this comparison are shown in a wider selection of samples: 5 independent MPNST cell lines, 3KO MSC ($n = 3$ biological replicates), 3KO NC ($n = 3$ biological replicates), WT MSC ($n = 3$ technical replicates), 1KO MSC ($n = 3$ biological replicates), 2KO MSC ($n = 1$), 2KO NC ($n = 3$ biological replicates), 1KO NC ($n = 3$ biological replicates), WT NC ($n = 3$ technical replicates) (See also Supplementary Data 3. **E** Biological processes identified by the enrichment analysis of genes in cluster N1 (see (**D**)). See also Supplementary Data 3. Dot plots show enriched GO Biological Process terms on the *y*-axis and gene ratio on the *x*-axis; dot size represents gene count and dot color represents the Benjamini–Hochberg-adjusted *p*-value. GO enrichment analysis was performed using a one-sided hypergeometric test. **F** Biological processes identified by the enrichment analysis of genes in cluster G (see (**D**)). See also Supplementary Data 3. **G** Heatmap showing the differential expression analysis of 3KO NC ($n = 3$ biological replicates) vs 5 independent MPNST cell lines in all samples (as in D). See also Supplementary Data 5. **H** Biological processes identified by the enrichment analysis of genes in cluster M (see (**G**)). See also Supplementary Data 5. **I** Biological processes identified by the enrichment analysis of genes in cluster N2 (see (**G**)). See also Supplementary Data 5. **J** Enrichment analysis of genes with differentially open (top) and closed (bottom) chromatin accessibility regions in PRC2-deficient NC cell lines ($n = 3$ biological replicates) compared to PRC2-WT NC ($n = 4$ biological replicates). See also Supplementary Data 6. **K** Correlation plot integrating differential gene expression and ATAC-seq data in PRC2-wild-type 1KO ($n = 2$ biological replicates), 2KO ($n = 2$ biological replicates) and PRC2-mutant 3KO NC ($n = 3$ biological replicates) cell lines. Cluster N1 and N2 neurogenesis signature genes highlighted in red; Cluster G gliogenesis signature highlighted in blue. The *x*-axis indicates ATAC-seq log fold change, and the *y*-axis indicates RNA-seq log fold change for the corresponding genes.

PRC2-null (3KO NC) and PRC2-WT (1KO and 2KO NC) supported the global opening of neurogenesis genes and the partial closing of gliogenesis genes (Fig. 5J, Supplementary Data 6). To complete this view, we plotted together gliogenesis and neurogenesis genes from clusters G, N1 and N2 (Fig. 5D–I), in a graph correlating gene expression and chromatin accessibility. Gliogenesis genes were downregulated, partly by epigenetic silencing, while neurogenesis-related genes were predominantly upregulated by an open chromatin conformation (Fig. 5K).

3KO neural crest cells recapitulate a glial-to-mesenchymal transition: gliogenesis impairment and expression of neuro-mesenchymal genes

We aimed to better understand the mechanisms driving this cell identity switch and its physiological implications. We first evaluated the ability of 3KO NCs to differentiate toward SCs, testing gliogenesis capacity. SC differentiation was induced in 1KO, 2KO, and 3KO NCs for 21 days[25] (Fig. 6A). 1KO and 2KO differentiating SCs exhibited both SOX9 and SOX10 expression, along with the SC lineage markers S100B and p75. Contrarily, 3KO differentiating cells preserved SOX9 expression but were not able to express SOX10, a master TF of gliogenesis, and any other SC marker, uncovering a loss of glial differentiation capacity. To determine whether *SOX10* inhibition was a direct epigenetic change produced by PRC2 loss, we analyzed chromatin accessibility in the *SOX10* promoter. We found a close chromatin conformation in 3KO NCs compared to the open conformation of 1KO and 2KO NCs (Fig. 6Bi), explaining the gliogenesis shutdown. In contrast, the *SOX9* TF promoter remained under an open chromatin conformation in 3KO NC cells (Fig. 6Bii).

Furthermore, to obtain a mechanistic insight into the expression of neuro-mesenchymal gene signatures identified and their importance to conform MPNST cell identity, we performed a global analysis of these signatures together with their chromatin accessibility status. Neurogenesis genes of cluster N1 (Fig. 5D, E) showed a consistent high expression in 3KO cell lines only—3KO NCs, 3KO MSCs and MPNST cell lines (Fig. 6Ci). In 3KO NCs, their promoters exhibited a differentially open chromatin conformation compared to PRC2-WT NCs (Fig. 6Di) and a positive correlation between chromatin opening and expression (Fig. 6Ei). Thus, these neurogenesis genes were poised by PRC2. Wound healing-related genes of cluster M (Fig. 5G, H) were only expressed in cells with mesenchymal identity, regardless of the genotype (Fig. 6Cii). Accordingly, although chromatin was preferentially open in 3KO NC vs PRC2-WT NCs (Fig. 6Dii), many of the genes did not change expression comparing all NC genotypes (Fig. 6Eii), indicating that their expression in MPNSTs is dependent on mesenchymal-related factors. Finally, another group of neurogenesis genes within the N2 cluster (Fig. 5G, I) was basically expressed only in MPNST cell lines (Fig. 6Ciii). Again, most of these genes opened their chromatin upon PRC2 loss in 3KO NCs (Fig. 6Diii), but many of them did not change the expression in 3KO NCs vs 2KO (Fig. 6Eiii). All together indicated that in addition to PRC2 loss and mesenchymal-associated factors, other genes, such as those of the cluster N2 signature, required additional unknown factors to be expressed in MPNSTs, also reinforcing neurogenesis as part of the MPNST cell identity. Chromatin accessibility and expression of representative genes of the different signatures are shown in Fig. 6F and Supplementary Fig. 8. Overall, results supported that NF1-associated 3KO MPNST identity is deeply influenced by losing glial differentiation capacity and the expression of developmental neuro-mesenchymal programs.

Glial-to-neuro-mesenchymal signatures identified in 3KO NCs also differentiate benign from malignant NF1-associated PNS tumors

We then assessed the relevance of the different signatures identified in the iPSC-derived NC models to the identity of the NF1-associated tumors and their benign-to-malignant progression, using global expression analysis. We first analyzed bulk RNA-seq data from primary PNF-derived SCs, PNFs, ANNUBPs, and MPNSTs, focusing on previously defined gliogenesis, neurogenesis genes and wound healing genes (Fig. 7A). Gliogenesis genes from cluster G were predominantly expressed in SCs and benign tumors. Cluster N1 neurogenesis genes segregated into three groups: (i) genes (e.g., *NGF*, *VIM*, *ITGA2*) upregulated in benign tumors and SCs; (ii) genes (e.g., *FOXD1*, *GATA3*, *PCSK1*) enriched in MPNSTs, absent in SCs and with low expression in PNFs/ANNUBPs, likely due to the presence stromal cells; and (iii) genes (e.g., *NKX2-2*, *PITX1*, *FOXG1*), along with Cluster N2 genes (e.g., *NR2E1*, *DMRT3*, *FOXB1*), expressed only in MPNSTs. Selected wound healing genes from cluster M (Supplementary Data 5, in bold) were also predominantly expressed in MPNSTs. These transcriptional profiles reflect a glial-to-neuro-mesenchymal transition underlying NF1 tumor progression.

Furthermore, we investigated this transition characterized by the identified signatures, using single-cell data obtained from nerves, PNFs, ANNUBPs and MPNSTs, to better understand their relevance but according to the different cell types within tumors (Fig. 7B). Expression of gliogenesis genes like *SOX10*, *NGFR* and *PLP1* identified in cluster G, was restricted to the glial component of all tissues and tumors analyzed, particularly expressed in ANNUBP samples (Fig. 7Bii). Contrarily, expression of identified neuro-mesenchymal genes from clusters N1,

https://doi.org/10.1038/s41467-026-73119-8

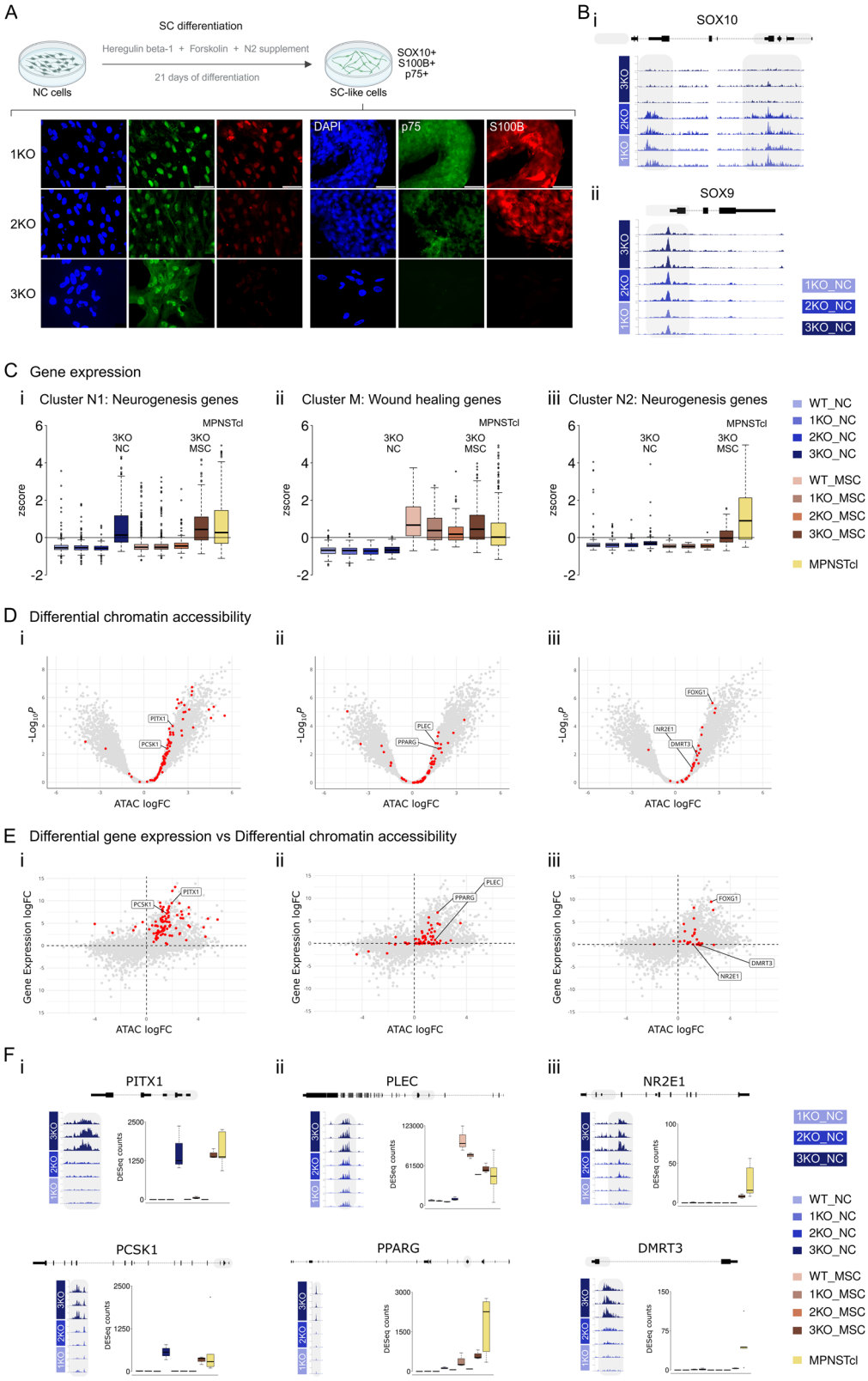

N2 and M, such as *PCSK1*, *PLEC* and *PPARG*, was restricted to the mesenchymal component of MPNSTs, like other MPNST markers like *SOX9*, *TWIST1* and *PRRX1* (Fig. 7Biii), further supporting the importance of identified gene signatures for MPNST identity. Single-cell data decomposed by a single tumor ($n = 16$) on the glial-to-neuro-mesenchymal transition markers studied was also performed to assess tumor diversity (Supplementary Data 7).

High-throughput screening of epigenetic modulators identifies candidate compounds and synergistic combinations with MEK inhibition in 3KO NC spheroid 3D model

After showing that the NC-based models developed mimic many features of malignant NF1-associated PNS tumors and considering the global epigenetic remodeling produced by PRC2 loss, we next used these NC models to identify epigenetic modulators as potential

Fig. 6 | Loss of SC differentiation capacity in 3KO NC cell lines due to *SOX10* epigenetic closure. Neurogenesis genes: part of MPNST cell identity. A NC-SC differentiation scheme and immunofluorescence images of SOX9, SOX10 and NC-SC markers (p75 and S100B) after 21 days of SC differentiation in 1KO, 2KO and 3KO cell lines ($n = 2$ independent experiments). Scale bar: 50 μm. Created in BioRender. Carrió, M. (2026) https://BioRender.com/rh6rwv6. **B** ATAC-seq chromatin accessibility plot in 1KO ($n = 2$ biological replicates), 2KO ($n = 2$ biological replicates) and 3KO ($n = 3$ biological replicates) cell lines of (**i**) *SOX10* locus, showing epigenetic silencing in 3KO cell lines and (**ii**) *SOX9* locus, showing no changes between NC cell lines. **C** Boxplot showing the expression z-score of (**i**) Cluster N1 neurogenesis gene signature ($n = 118$ genes) (Fig. 5D, E); (**ii**) Cluster M wound healing gene signature ($n = 73$ genes) (Fig. 5G, H); (**iii**) Cluster N2 neurogenesis gene signature ($n = 34$ genes) (Fig. 5G, I). Samples are 5 independent MPNST cell lines, 2KO MSC ($n = 1$), WT MSC ($n = 3$ technical replicates), and 3 biological replicates of WT NC, 1KO NC, 2KO NC, 3KO NC, 1KO MSC, 3KO MSC. Boxplots show the median (center line), upper and lower hinges (box limits), and whiskers extending to the most extreme value within 1.5× the interquartile range from the hinges; points beyond the whiskers are shown individually as outliers. **D** Volcano-plot showing differential chromatin accessibility of PRC2 WT 1KO NC ($n = 2$ biological replicates) and 2KO NC ($n = 2$ biological replicates) compared to PRC2-null 3KO NC ($n = 3$ biological replicates). (**i**) Cluster N1 neurogenesis genes ($n = 97$) highlighted in red; (**ii**) Cluster M wound healing genes ($n = 73$) highlighted in red; (**iii**) Cluster N2 neurogenesis genes ($n = 30$) highlighted in red. The *x*-axis shows log2 fold change and the *y*-axis shows −log10 *p*-value for each feature. Differential accessibility was assessed with edgeR performing a quasi-likelihood test relative to the fold change. **E** Correlation plot integrating differential gene expression and ATAC-seq data in PRC2 WT 1KO NC ($n = 2$ biological replicates) and 2KO NC ($n = 2$ biological replicates) compared to PRC2-null 3KO NC ($n = 3$ biological replicates). (**i**) Cluster N1 neurogenesis genes ($n = 97$) highlighted in red; (**ii**) Cluster M wound healing genes ($n = 73$) highlighted in red; (**iii**) Cluster N2 neurogenesis genes ($n = 30$) highlighted in red. The *x*-axis indicates ATAC-seq log fold change, and the *y*-axis indicates RNA-seq log fold change for the corresponding genes. **F** ATAC-seq chromatin accessibility plot in 1KO, 2KO and 3KO cell lines and normalized expression in all cell lines of (**i**) *PITX1* and *PCSK1* genes from Cluster N1 neurogenesis genes; (**ii**) *PLEC* and *PPARG* genes from Cluster M wound healing genes; (**iii**) *NR2E1* and *DMRT3* genes from Cluster N2 neurogenesis genes. Samples for ATAC-seq as in (**B**), and samples for expression as in (**C**). Boxplots show the median (center line), upper and lower hinges (box limits), and whiskers extending to the most extreme value within 1.5× the interquartile range from the hinges; points beyond the whiskers are shown individually as outliers.

therapies for MPNST treatment. We conducted a quantitative high-throughput screen (qHTS) using the NCATS Pharmacologically Active Chemical Toolbox (NPACT) Epigenetics library, comprising 339 small-molecule modulators of epigenetic targets (Supplementary Fig. 9A, B, Supplementary Data 8). We used the different NC models developed (1KO, 2KO, 3KO) grown as 3D spheroids and an additional 3KO cell line carrying a heterozygous *TP53* background (3KO+) since *TP53* is mutated in some MPNSTs (Supplementary Figs. 9, 10). We tested the compounds in dose-response across all 3D NC spheroid models and measured cell viability with CellTiter-Glo 3D (CTG) after 48 h of treatment. Spheroids of NF1 patient-derived fibroblasts were used for assessing general toxicity (Supplementary Figs. 9, 11). We confirmed that these spheroid models generated robust assays, with Z′-factor values across all cell lines ranging between 0.75 and 0.82 (Supplementary Table 1). In general, a large subset of compounds (250/339) showed no activity in 3KO cell lines ($IC_{50} \geq 13$ μM) or showed poor or ambiguous dose-response curves (224/339). Of the 339 compounds tested, 15 showed broad cytotoxicity (Fig. 8A, Supplementary Data 9).

Based on the initial qHTS curve classifications, we selected compounds displaying activity profiles (curve response class (CRC) values of −1.1, −1.2, −2.1, or −2.2)[26] together with high potency ($IC_{50} < 13$ μM) and spheroid morphology changes (Fig. 8B), as well as a few generally cytotoxic compounds, as toxicity controls. We selected 77 compounds and performed 11-point dose-response curves to refine IC_{50} estimations (Supplementary Data 12) and also performed live-cell imaging (live/dead assays) to evaluate morphological changes not captured by CTG (Supplementary Fig. 12). Interestingly, although changes in the IC_{50} value were generally below threefold, nearly all BET inhibitors (BETi) exhibited greater activity in 1KO and 2KO cells compared to 3KO and 3KO+ cells (Fig. 8C). However, as for most compounds, HDAC inhibitor (HDACi) Belinostat and BETi I-BET151 exhibited comparable effects across all four isogenic lines (Fig. 8C, Di, ii). In contrast, selective loss of viability for PRC2-deficient spheroids was observed for PARP inhibitors (PARPi), with 3 out of 4 PARPi showing more than a threefold change in IC_{50} in PRC2-mutant cells compared to PRC2 WT cells (Fig. 8C). As an example, the effects of Olaparib are illustrated in Fig. 8Diii. Additional effects were evident across several compounds (Supplementary Fig. 13).

Given the well-documented poor efficacy of monotherapies for MPNST treatment, particularly in vivo, we performed combination testing using 48 selected epigenetic compounds with Selumetinib in a 6 × 6 matrix format in 3KO NC and control fibroblasts spheroids (Supplementary Data 12). As single agents, neither Selumetinib, a clinically approved treatment for PNFs, nor Ribociclib (a CDK4/6 inhibitor, CDKi) exhibited a robust dose-response activity in the 3KO NC model (Supplementary Fig. 14), consistent with observations reported for other MPNST models[27–30]. However, combinations of Selumetinib and BETi, HDACi, AURKA/Bi, or PARPi, indicated slight synergistic effects, as measured by analyses using both DBSumNeg and Excess Highest Single Agent (HSA) (Supplementary Fig. 15A, B, Supplementary Data 12), consistent with previous results for some of these combinations[13,31,32].

We next performed an in-depth assessment of combination effects with a reduced number of compound combinations across multiple cell lines, including the three isogenic 3KO lines (3KO_H8, 3KO_C6 and 3KO_D8) and three established MPNST lines (STS88-14, sNF96.2, NMS-2), thus covering models representing both an early-stage MPNST development (3KO NC spheroids) and late stage (2D MPNST cell lines) (Supplementary Fig. 16A). We prioritized non-toxic combinations: PARPi (Olaparib, Talazoparib), the least toxic HDACi (Entinostat, Belinostat, ACY-1215) and BETi (I-BET151, GSK1324726A, Alobresib, CPI-0610) (Supplementary Fig. 16B).

While both HDACi and BETi combinations with Selumetinib reduced viability across all models (Fig. 8Ei, ii, Supplementary Fig. 18A, B), PARPi effects were restricted to 3KO NC spheroids, with minimal impact on MPNST cell lines (Fig. 8Eiii, Supplementary Fig. 17A–C). HDACi combinations with Selumetinib were generally toxic, narrowing the potential therapeutic window (Supplementary Figs. 17C, 18A), and BETi combos showed some toxicity at higher concentrations (Supplementary Figs. 17C, 18B). Dose-response curves were highly consistent across replicates, underscoring the reproducibility of the assays. To further assess potential synergistic effects with Selumetinib, combination index (CI) and fraction affected (Fa) values were calculated using three concentrations above and below the IC_{50} of the compounds in 3KO_H8. For both I-BET151 and Belinostat, most CI values were below 0.9, indicating synergy in both models (Fig. 8Fi, ii). In contrast, nearly none of the combinations of Selumetinib with PARP inhibitors exhibited clear synergistic effects in MPNST cell lines, with most CI values exceeding 1.5 (Fig. 8Fiii, Supplementary Fig. 17B) but indeed reached CI values below 0.6–0.9 in 3KO NC spheroids.

Pilot in vivo study using NF1 MPNST PDOX identifies Olaparib-based combinations as a potential therapeutic strategy for MPNSTs

Given the observed selectivity of PARPi-Selumetinib co-treatments across the 3KO NC in vitro models, we evaluated the efficacy of

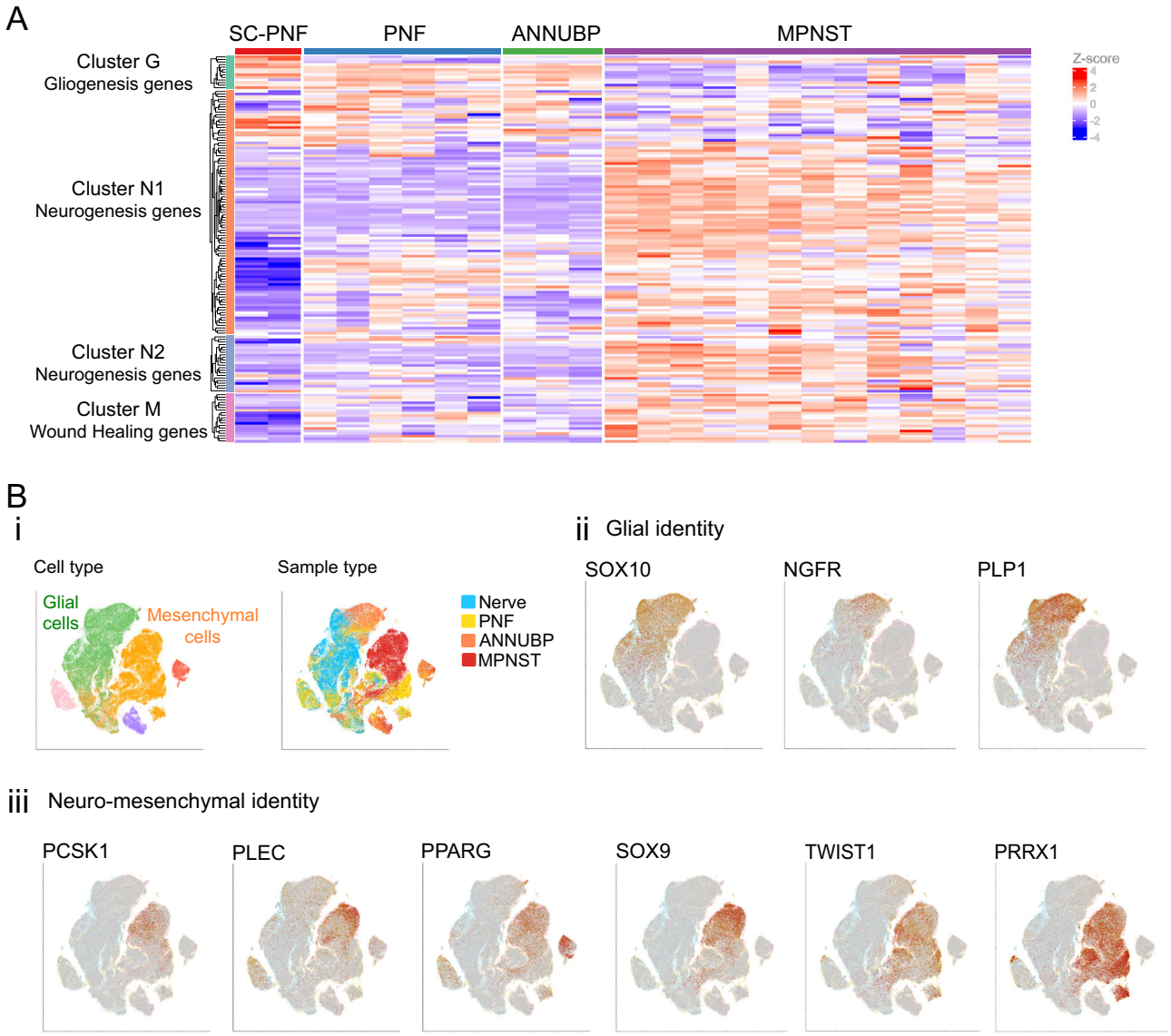

Fig. 7 | Glial to neuro-mesenchymal transition in human NF1-related tumors. **A** Heatmap showing identified gliogenesis and neurogenesis gene signatures across human NF1-associated PNF-SCs ($n = 2$ independent PNF-derived primary SC), PNF ($n = 6$ independent human tumors), ANNUBP ($n = 3$ independent human tumors), and MPNST ($n = 13$ independent human tumors) samples. **B** TSNE plots representing single-cell RNA-seq data from nerve ($n = 4$ independent healthy nerve samples), PNF ($n = 5$ independent human tumors), ANNUBP ($n = 4$ independent human tumors) and MPNST ($n = 3$ independent human tumors) samples. (**i**) Representation of cell type composition and sample type distribution. (**ii**) Gliogenesis genes *SOX10*, *NGFR* and *PLP1* are exclusively expressed in de glial cell component. (**iii**) Neurogenesis gene (*PCSK1*) and mesenchymal genes (*PLEC*, *PPARG*, *SOX9*, *TWIST1* and *PRRX1*) are exclusively expressed in mesenchymal cells and mostly in MPNSTs.

Olaparib in combination with Selumetinib, Ribociclib, or I-BET151, in an MPNST PDOX model (NF1-18B) described recently[31,33].

A pilot exploratory in vivo treatment consisted of groups of 5–8 mice (52 animals), mixing females and males, that, after PDOX formation, were treated for 21 days with distinct compounds and combinations. We used Olaparib in double and triple combinations with Selumetinib (MEKi), and Ribociclib (CDKi) or I-BET151 (BETi), which were compared to vehicle-treated control, Olaparib as a single agent and the triple MEKi-CDKi-BETi combination as the combination that elicited the greatest response in the NF1-18B PDOX model so far (Fig. 9A)[31]. Treatment conditions are detailed in Supplementary Fig. 19A. Body weight was monitored daily to asses toxicity throughout the 21-day treatment period, with no weight loss detected (Fig. 9B). Relative tumor volume for each mouse was also recorded (Fig. 9C). At the end of the treatment, mice were euthanized, and tumors were photographed (Supplementary Fig. 19B) and weighed (Fig. 9D) to compare treatment efficacy. In addition, liver, kidney, lung, and heart tissues were collected and analyzed by hematoxylin and eosin (H&E) and Masson's trichrome staining. No evidence of tissue damage, inflammation, necrosis, or fibrosis was observed (Supplementary Figs. 20, 21).

Overall, single-agent Olaparib treatment did not change tumor volumes and growth kinetics compared to vehicle controls, indicating minimal anti-tumor activity. In contrast, all tested double combinations with Olaparib resulted in substantial reductions in relative tumor volume, as well as in tumor weight, compared with vehicle controls: Olaparib/I-BET151 achieved a 30.6% reduction, Olaparib/Ribociclib a 36.5% reduction, and Olaparib/Selumetinib a 61.6% reduction that was also statistically significant, suggesting an apparent therapeutic benefit (Fig. 9C–E). Triple combinations of Olaparib, Selumetinib and a Ribociclib or I-BET151 did not enhance tumor reduction compared to double treatments (Fig. 9C). Despite the limitations of this pilot in vivo

https://doi.org/10.1038/s41467-026-73119-8

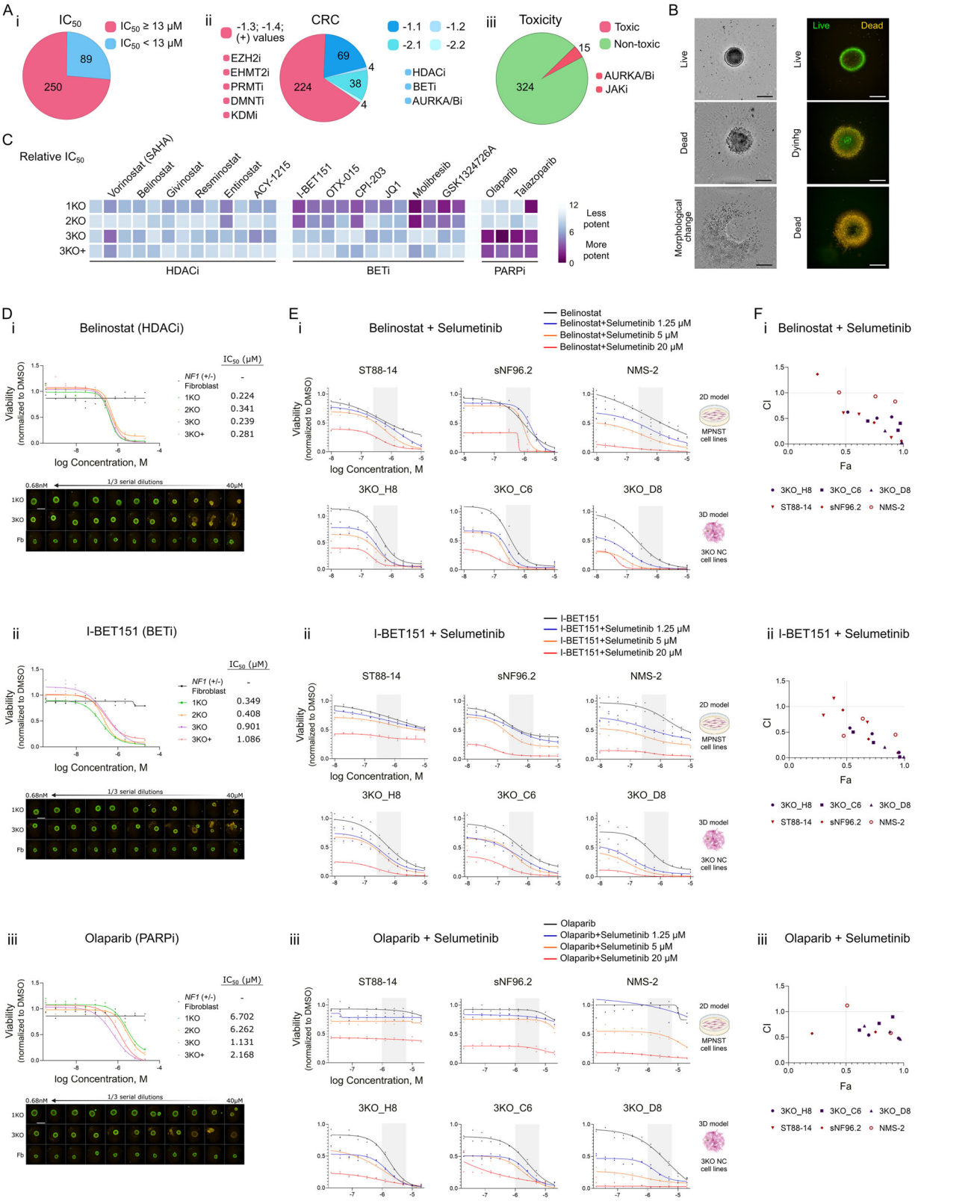

study, the Olaparib/Selumetinib combination yielded the most significant reduction in tumor weight (Fig. 9D), close to the effect of the triple MEKi-CDKi-BETi combination, emerging as the most effective regimen from this work. However, as previously mentioned, both male and female mice were included in the study, and we identified different treatment responses according to mice sex (Supplementary Fig. 19C–E), which need to be explored in more detail.

Focusing on the favorable outcomes observed with the double-treatment regimens (Fig. 9E) and comparing them with controls, we performed Western blot (WB) analyses in resected tumors at the end of the treatment, for each double combination to assess target engagement and downstream pathway effects (Rb, Myc and ERK) as described previously[31] and PARP1 PARylation for PARPi, with loss of PARylation indicating target engagement[34]. WB and their quantification (Fig. 9F, G,

Fig. 8 | High-throughput screening and validation of epigenetic compound modulators, as single agents and in combination with Selumetinib (MEKi), in isogenic 3KO NC spheroid models and MPNST cell lines. A Summary of qHTS results presented as pie charts. (**i**) Activity: classification based on IC_{50} and CRC values in 3KO spheroids. Active compounds (blue): CRC −1.2, −1.2, −2.1 and −2.2; and $IC_{50} < 13$ μM. Inactive compounds (red): CRC −1.3, −1.4 and positive values; and $IC_{50} \geq 13$ μM. (**ii**) Toxicity: compounds with $IC_{50} < 1$ μM in control fibroblast spheroids or similar IC_{50} values across all cell lines (IC_{50} in isogenic spheroids > 5-fold IC_{50} in the fibroblast control spheroids). See also Supplementary Data 10. Created with BioRender.com. **B** Representative phase contrast (left) and Live/Dead fluorescence (right) micrographs of 3KO spheroids after 48 h of treatment ($n = 1$ experiment). See also Supplementary Fig. 12. Scale bar: 250 μm. **C** Heatmap showing the relative IC_{50} of BETi, PARPi and HDACi across isogenic cell lines. Dark purple indicates higher potency ($n = 2$ independent experiments) (row data in Supplementary Data 11). Created with BioRender.com. **D** Upper panel: Dose-response CellTiter-Glo (CTG) cell viability graphs of the four isogenic NC cell lines and control fibroblasts, grown in 3D, together with corresponding IC_{50} values. Data correspond to eleven dose-response concentrations, from two independent replicates. Bottom panel: Live/dead micrographs for each dose in 1KO, 3KO, and control fibroblasts (Fb). Scale bar: 500 μm. **E** Dose-response CTG cell viability plots of candidate compounds in combination with Selumetinib (MEKi) for each 3KO NC and MPNST cell lines. Shaded areas indicate three concentrations above and below the IC_{50} of the compounds in 3KO_H8 used to calculate the combination index (CI). Data correspond to eleven dose-response concentrations; each point shows the mean ± SD from two independent replicates. Created in BioRender. Carrió, M. (2026) https://BioRender.com/pforv4l. **F** CI plots of the shaded doses (two independent replicates) from (**E**), showing the fraction affected (Fa) versus CI for the 3KO (purple) and MPNST (red) cell lines. Fa represents the fraction of cell death induced by drug treatment, ranging from 0 (no cell death) to 1 (complete cell killing). CI values < 0.9 indicate a synergistic interaction, values between 0.9 and 1.1 indicate an additive effect, and values >1.1 indicate antagonism. Source data are provided as a Source Data file.

respectively) confirmed the on-target activity of the different compounds within tumors, reaching statistical significance in all cases except for the reduction in c-MYC expression. In addition, WB analysis showed increased BIM levels in treated tumors, suggesting pro-apoptotic pathway activation, although without statistical significance (Supplementary Fig. 19F).

Taken together, these results indicate that our iPSC-derived NC models provide a valuable platform for drug screening with a good agreement with in vivo results and support the potential efficacy of PARPi-MEKi or PARPi-CDKi, as a therapeutic option for MPNSTs.

Discussion

We studied the role of the most commonly inactivated TSGs in the early development of MPNSTs using an iPSC-derived NC model system and sequentially inactivating *NF1*, *CDKN2A* and *SUZ12*, to mimic the benign-to-malignant transition during PNF-ANNUBP-MPNST progression.

It is now well established that the loss of *CDKN2A* in *NF1*(-/-) PNF cells is the trigger for ANNUBP formation[6,7], becoming a pre-malignant lesion difficult to manage in the clinic due to the lack of tools for risk assessment[10,11,35]. In our NC models, 2KO NCs retain glial differentiation capacity and form neurofibroma-like lesions when engrafted in the sciatic nerve of nude mice. However, no histological atypia was detected in these neurofibromas, suggesting that a longer period of tumor development might be necessary. *CDKN2A* inactivation did not affect cell cycle or proliferation rate at iPSC and NC stages, but led to gene expression changes when compared to 1KO NCs. One of the differentially expressed genes was *TYMS,* which is also differentially overexpressed in ANNUBPs compared to PNFs. *TYMS* inhibitors, like Pemetrexed, exist and have been used to inhibit proliferation in cells deficient in *CDKN2A*[23]. Our results show the existence of a window of opportunity for *TYMS* inhibition in ANNUBPs, although further experiments are required to confirm this possibility.

CDKN2A encodes p14ARF and p16INK4a. Different genetically modified mouse (GEM) models have shown that the loss of *NF1* and *CDKN2A* is required for ANNUBP formation[16,17], some pointing to p14ARF as the key *CDKN2A* gene. Our results demonstrate that wild-type p14ARF function impeded the proper formation of tumors in vivo, but also support the necessity of losing both genes for ANNUBP development, as it is seen in MPNST cell lines and human MPNST[24,36].

PRC2 function helps maintain cell identity through transcriptional repression driven by closed chromatin[37] and has been involved in many types of cancer[12]. Our work supports that the order of TSG inactivation in the PNF-ANNUBP-MPNST progression is biologically constrained. That would explain why neurofibromas in *NF1* patients carrying a constitutional microdeletion involving *NF1* and *SUZ12* never exhibit LOH[38]: PRC2 loss would activate p14ARF/p16INK4a expression through chromatin accessibility, inducing senescence[39,40].

We demonstrate that the NC models (1KO, 2KO, 3KO) developed here capture a benign-to-malignant transition and a change in cell identity caused by PRC2 inactivation. PRC2 loss causes a global chromatin remodeling largely affecting genome methylation and transcription, in a programmed and reproducible manner, since the three independent 3KO NC lines exhibit almost identical methylomes and transcriptomes. Mimicking the glial-to-mesenchymal transition observed from ANNUBP toward MPNST, 3KO NCs acquired a mesenchymal identity, consistent with previous results[41]. Previous studies have shown the role of PRC2 in the acquisition of mesenchymal characteristics by comparing MPNSTs with proficient and deficient PRC2, or re-expressing or deleting PRC2 components in MPNST or immortalized SC cell lines[42–44]. Here, we instead start from iPSCs to model stepwise TSG loss in NCs, a cell type close to the PNF/MPNST cell of origin, to investigate early tumorigenesis. We show that PRC2 loss changes cell identity by precluding gliogenesis capacity of 3KO NCs and activating the expression of neuro-mesenchymal programs.

Gliogenesis is impeded by the epigenetic silencing of *SOX10*, a master regulator TF[45], upon closing chromatin accessibility. This supports previous findings in MPNSTs were *SOX10* was found downregulated and epigenetically silenced when compared to benign tumors, and downregulated after PRC2 inactivation in MPNST cell lines[41,42,44,46]. On the other hand, the absence of PRC2 triggers the expression of repressed neuro-mesenchymal gene programs by the opening of chromatin accessibility. 3KO NC express mesenchymal and stemness genes like *SOX9*, *TWIST1* and *PRRX1* and neurogenesis-associated transcriptional programs consistent with previous observations[8,42,43,47]. The combined analyses of expression and chromatin accessibility, comparing 2KO with 3KO NCs on one hand, and 3KO NCs with MPNST cell lines (and MSCs) on the other, allowed the identification and characterization of these neuro-mesenchymal signatures. We identified PRC2 poised neurogenesis genes that are immediately expressed after PRC2 loss, likely due to loss of REST–PRC2 repression[48], remaining active in MPNST cells. Other mesenchymal and neurogenesis genes may adopt an open chromatin conformation, or already have it, but 3KO NCs lack other necessary factors for their expression, some mesenchymal-associated present in MSCs and MPNST cell lines, and other unknown and only present in MPNSTs (perhaps associated with genomic alterations), driving the expression of additional neurogenesis genes. These identified gliogenesis, neurogenesis and mesenchymal signatures reproduced the glial-to-neuro-mesenchymal transition when analyzed in human tumors representing the PNF-ANNUBP-MPNST malignant progression.

The reproduction of this cell identity transition during malignant progression, together with the capacity of 3KO NC spheres of generating histologically compatible early MPNST-like tumors in

https://doi.org/10.1038/s41467-026-73119-8

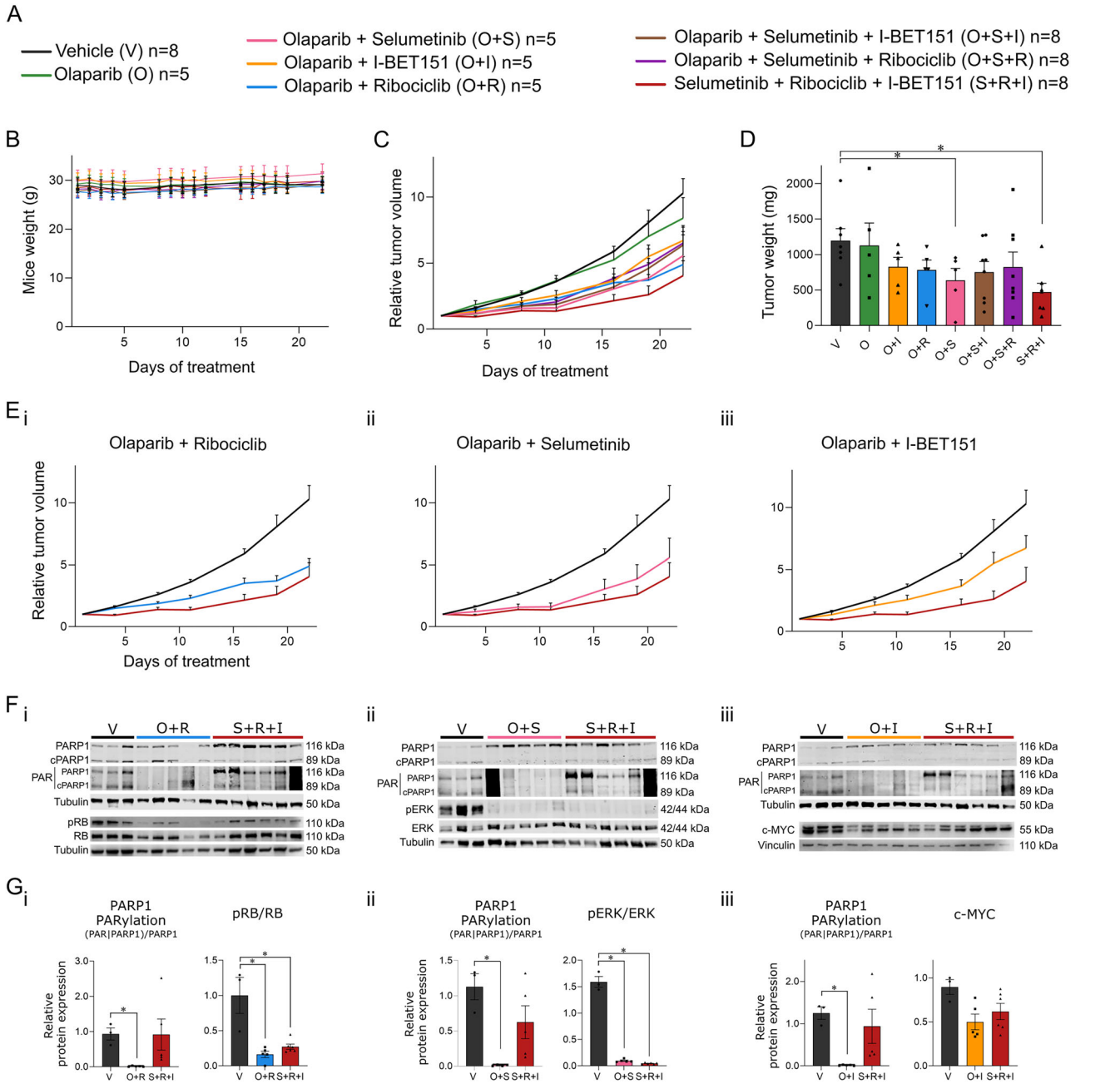

Fig. 9 | In vivo evaluation of Olaparib (PARPi) alone and in double or triple combinations with Selumetinib (MEKi) and Ribociclib (CDKi) or I-BET151 (BETi) in the NF1-associated NF1-18B MPNST PDOX mouse model. A List of single, double, and triple treatment combinations used in the study, with each combination color-coded; *n* indicates the number of mice used for each experimental condition. **B** Plot showing mice weight during the 3 weeks of treatment. Data are presented as mean values ± SEM from each experimental group. **C** Relative tumor volume growth of the NF1-18B PDOX mouse model in each treatment group over the course of the study. Data are presented as mean values ± SEM. **D** Tumor weight at the end of the experiment. Each black dot indicates one single value. Mann–Whitney two-tailed test; $^*p \le 0.05$. Exact *p*-values and Source data are provided as a Source Data file. **E** Relative tumor volume growth for double combination groups, V (negative control) and triple S + R + I combination (positive control) throughout the experiment. (**i**) O + R; (**ii**) O + S; (**iii**) O + I. Data are presented as mean values ± SEM. **F** Western blot images of readouts of the molecular targets of Olaparib (PARP1 PARylation), Selumetinib (p-ERK/ERK), Ribociclib (p-RB/RB), and I-BET151 (c-MYC). V ($n = 3$ tumors analyzed); O + S ($n = 5$ tumors analyzed); O + I ($n = 5$ tumors analyzed); O + R ($n = 5$ tumors analyzed); and S + R + I ($n = 6$ tumors analyzed). (**i**) O + R; (**ii**) O + S; (**iii**) O + I. The samples derive from the same experiment but different gels for PARP1, PAR, another for RB, another for pRB, another for p-ERK, ERK, and another for MYC were processed in parallel. **G** Quantification of molecular targets by Western blot from (**F**). (**i**) O + R; (**ii**) O + S; (**iii**) O + I. Mann–Whitney two-tailed test; $^*p \le 0.05$. Data are presented as mean values ± SEM. Exact *p*-values and Source data are provided as a Source Data file. V: vehicle, O: Olaparib, S: Selumetinib, I: I-BET151, R: Ribociclib.

mice upon engraftment, reinforces the validity of these cells as a genuine MPNST model. This is an in vitro/in vivo genetically engineered MPNST model incorporating the loss of all three TSGs implicated in PNF-to-MPNST progression that can still be further developed. Despite being diploid, the resulting tumors are hypercellular and proliferative, but lack the aggressiveness of MPNST PDOX models[33], consistent with an early developmental stage. The genes exclusively expressed in MPNST cell lines (not in 3KO NCs, neither in 3KO MSCs) could play a role in providing this malignant behavior.

We then set up the 3KO NC MPNST spheroid model to be highly scalable, rapid, and reproducible, providing a robust platform for high-throughput drug screening (HTS). Because PRC2 loss has a great impact on chromatin, we tested a large library of compounds targeting epigenetic modifiers, identifying those inhibiting BET, HDAC and AURKA/B as active agents, which had already been identified as potential treatments for MPNST[13,20,33,49–51]. However, most compounds inhibiting these targets were not selective for 3KO NCs. On the other hand, poly(ADP-ribose) polymerase inhibitors (PARPi) exhibited a preferential activity against PRC2-deficient spheroids, even though they were not as effective against MPNST cell lines in 2D. The combination of Olaparib-selumetinib was synergistic in 3KO spheroid models and was well tolerated and significantly inhibited tumor growth in vivo in a patient-derived orthotopic xenograft MPNST mouse model. This result would have remained undetected if the HTS had been done using MPNST cell lines in the usual 2D cell growth assays. Further in vivo studies are needed to better characterize the beneficial effects of this co-treatment, including optimizing MEKi and PARPi dosing regimens.

Several studies have explored potential combinations of PARPi with MEKi, CDKi, and BETi in different tumor types[52–56]. In fact, PARPi has already been proposed as a therapeutic agent for MPNSTs[57] although this line of research has been scarcely followed, only by Larsson and colleagues (2023)[58]. Here, we uncover the combination of PARPi and Selumetinib as a therapeutic option for MPNST.

The NC spheroid system provides a representative model of PNF-ANNUBP–MPNST progression to investigate MPNST initiation mechanisms and malignant properties. It also serves as a robust platform for compound screening, bridging in vitro studies with in vivo validation and enabling the identification of combinatorial strategies for MPNST therapy.

Methods

Ethical compliance

This study complied with all relevant ethical regulations. The use of induced pluripotent stem cells (iPSCs) in this study was approved by the competent Spanish authorities (Commission on Guarantees concerning the Donation and Use of Human Tissues and Cells of the Carlos III Spanish National Institute of Health). The human research protocol was approved by the Clinical Research Ethics Committee of Germans Trias i Pujol Hospital, Badalona, Spain, Project No PI-19-124. All mouse experiments were conducted in accordance with relevant Spanish national laws (RD 1201-/2005) and international guidelines and regulations (European Union rules 2010/63/UE), about the protection of animals used for experimentation and other scientific purposes. The experimental protocols were approved by the IDIBELL Animal Ethic Experimentation Committee (CEEA-IDIBELL approval No 9111) in Spain. They complied with the International Association for Assessment and Accreditation of Laboratory Animal Care procedures (AAALAC).

Human iPSC lines

The following human induced pluripotent stem cell (hiPSC) lines were utilized in this study: FiPS Ctrl1-SV4F-7 used as a control *NF1*(+/+) cell line and named WT in this article, and *NF1*(-/-) edited FiPS Ctrl1-SV4F-7, previously generated in our lab[21] and named 1KO_D12 in this article. These lines are banked and stored at the Spanish National Stem Cell Bank, Institute of Health Carlos III (BNLC-ISCIII). The iPSC lines used were authenticated by PCR-based DNA fingerprinting analysis using the AmpFlSTR_IdentifilerTM PCR Amplification Kit panel from Applied Biosystems.

Human iPSCs were cultured on Growth Factor Reduced Matrigel (Corning) in mTeSR media (StemCell Technologies), and maintained at 37 °C in a 5% CO_2 atmosphere. Passage of cells, when necessary, was performed using Accutase (Thermo Fischer Scientific).

Human cell lines

Three MPNST cell lines were used: sNF96.2 (RRID: CVCL_K281), ST88-14 (RRID: CVCL_8916), and NMS-2 (RRID: CVCL_4662). The human NF1 patient-derived fibroblast cell line (Coriell #GM00622) was used as a control cell line. ST88-14, sNF96.2 and NF1 fibroblasts were maintained in DMEM (Gibco) + 10% FBS (Gibco) + 2 mM GlutaMAX (Gibco) + 100 U/mL penicillin/100 mg/mL streptomycin (Gibco). NMS-2 cell line was maintained in RPMI (Gibco) + 10% FBS + 2 mM GlutaMAX + 100 U/mL penicillin/100 mg/mL streptomycin. All cell lines were incubated at 37 °C with 5% CO_2.

CRISPR/Cas9 gene edition

We generated *NF1*(-/-) *CDKN2A* p14ARF(+/+)p16INK4a(-/-) iPSC lines (referred to as 2KO (p16)) and *NF1*(-/-) *CDKN2A* p14ARF(-/-) p16INK4Aa(-/-) iPSC lines (referred to as 2KO (p14p16)) through CRISPR/Cas9 gene editing of the *NF1*(-/-) edited FiPS Ctrl1-SV4F-7 (referred to as 1KO cell line) using the ArciTect ribonucleoprotein (RNP) system from StemCell Technologies. We next edited *SUZ12* in the 2KO_F9 iPSC line, generating *NF1*(-/-) *CDKN2A* p14ARF(-/-) p16INK4a(-/-) *SUZ12*(-/-) cells (referred to as 3KO). We also edited the *TP53* gene in 3KO NC cells (3KO_H8 cell line), generating a *NF1*(-/-) *CDKN2A* (-/-) *SUZ12* (-/-) *TP53* (+/-) NC line (referred to as 3KO+). Briefly, sgRNAs targeting exon 2 of the *CDKN2A* gene for 2KO (p16) and for 2KO (p14p16), exon 1 and exon 10 of the *SUZ12* gene were introduced into hiPSCs (Supplementary Data 1). In the case of the *TP53* gene, sgRNAs targeting exon 5 were introduced into NCs (Supplementary Data 1). In all cases, sgRNAs were introduced using TransIT-X2 transfection reagent (Mirus), following the manufacturer's instructions. Single-cell clones were amplified, and DNA was extracted for *CDKN2A*, *SUZ12* and *TP53* mutation analysis using DNA Sanger sequencing. For the sequencing of each allele, the Gateway Technology cloning method (Invitrogen) was employed using the pDONR 221 vector. Sequences were analyzed using CLC Workbench 8 software (Qiagen). Primers used for sequencing can be found in Supplementary Data 1.

iPSC differentiation toward neural crest (NC)

iPSCs were differentiated toward a neural crest (NC) lineage using a previously established approach[25]. Cells were cultured in NC induction medium composed of a 1:1 mixture of DMEM (Gibco) and F12 (Gibco) supplemented with 5 mg/mL bovine serum albumin (Sigma), 100 U/mL penicillin/100 mg/mL streptomycin (Gibco), 2 mM GlutaMAX (Gibco), 1X non-essential amino acids (Gibco), 1X trace element solutions (A, B, and C) and 90 μm 2-mercaptoethanol. Additional components included 10 μg/mL Apo-transferrin (Sigma); 50 μg/mL sodium L-ascorbate (Sigma); 10 ng/mL Heregulin-b1 (PeproTech); 200 mg/mL LONG R3 IGFR (PeproTech); 8 ng/mL basic fibroblast growth factor 2 (PeproTech), 2 μM CHIR9902 (STEMCELL Technologies) and 20 μM SB432542 (STEMCELL Technologies). Cells were maintained in this medium and passaged using Accutase when reaching appropriate confluency.

Spheroid generation from neural crest (NC)

For engraftment experiments, neurofibromasphere generation of 1KO and 2KO cells was performed as reported before[21,22]. For 3KO cells, 1.2×10^6 NC cells were seeded into AggreWell™ 800 plates pre-treated with Anti-Adherence Rinsing Solution (STEMCELL Technology) in NC media. 48 h later, spheroids were collected and engrafted into the sciatic nerve of nude mice.

For HTS experiments, 3×10^3 NC cells or 2×10^3 *NF1*(+/-) fibroblasts were seeded per well in 384-well, round-bottom, ultra-low attachment (ULA) plates (Corning), centrifuged at 300×*g* for 5 min and incubated at 37 °C. Spheroids were treated with compounds at 24 h post-seeding, and downstream functional assays were performed at 48 h.

Neural crest (NC) differentiation toward Schwann cells (SCs) and mesenchymal stem cells (MSC)

SC differentiation was performed as reported previously[25]. Briefly, 4 × 10^4 NC cells per cm^2 were plated onto 0.1 mg/mL Poly-L-lysine (Sigma) and 4 μg/mL Laminin (Gibco)-coated plates and cultured in SC differentiation medium: DMEM:F12 (3:1); 100 U/mL penicillin/100 mg/mL streptomycin; 1% FBS; 5 μM Forskolin (Sigma); 50 ng/mL Heregulin β1 (Peprotech); and 2% N2 supplement (Gibco). The medium was replaced twice a week. For MSC differentiation, NC cells were plated at a density of 6.5 × 10^4 cells per cm^2 in DMEM + 10% FBS + 100 U/mL penicillin/100 mg/mL streptomycin + 2 mM Glutamax-I + 90 μm 2-bmercaptoethanol (Gibco) onto noncoated tissue culture plates following previously reported protocols[59]. Cells were passaged every 4–5 days using trypsin-EDTA (Gibco).

Animal models

Male and female Foxn1nu (Harlan) nude mice (5 weeks of age) were housed under specific pathogen-free conditions in ventilated isolators. Environmental parameters were controlled with a 12-h light/dark cycle, temperature maintained at 22 °C, and relative humidity at ~55%. Animals had unrestricted access to autoclaved standard and acidified drinking water.

Engraftment experiments

For 1KO and 2KO cells, neurofibromaspheres were engrafted following previously reported protocols[21,22]. For 3KO cell lines, spheroids containing approximately 2 million cells were resuspended in 1:2 diluted Growth Factor Reduced Matrigel (Corning) in a total volume of 70 μL of NC medium and injected into the exposed sciatic nerve of 5-week-old nude mice using a 25 G syringe. We injected 1KO, 2KO_C4 and 2KO_F9 cell lines (8 mice per model) and the three 3KO cell lines (3KO_C6, 3KO_H8 and 3KO_D8) (12 mice total). Tumor growth was monitored by manual palpation, and after 4 months, mice were euthanized and tumors fixed in formalin for paraffin embedding.

Western blot

For protein extraction, cultured cells were lysed in RIPA buffer containing 50 mM Tris-HCl (pH 7.4), 150 mM NaCl (Merck), 1 mM EDTA (Sigma), 0.5% Igepal CA-630 (Sigma) supplemented with 3 mM DTT (Thermo Fisher), 1 mM PMSF (Sigma), 1 mM sodium orthovanadate (Sigma), 5 mM NaF (Sigma), 10 μg/mL leupeptin (Sigma), 5 μg/mL aprotinin (Sigma) and 1xPhosSTOP (Roche). Protein concentrations were determined, and equal amounts (90 μg) were resolved by SDS–PAGE, followed by transfer to PVDF membranes. Membranes were blocked and incubated with primary antibodies against NF1 (1:1000, Berthyl Laboratories) or p16INK4a (1:2000, Abcam) overnight at 4 °C, while α-tubulin (1:4000, Sigma) was used as a loading control. Detection was performed using infrared dye–conjugated secondary antibodies and visualized on an Odyssey CLx system.

For tumor-derived samples, proteins were isolated from 15–20 mg of tissue homogenized mechanically and clarified by centrifugation. Lysates (20 μg) were separated by SDS–PAGE and transferred to PVDF membranes. Immunodetection was carried out using either chemiluminescent substrates or fluorescence-based detection depending on the target protein, including Phospo-Rb Ser780 (1:1000, Cell Signaling), Rb 4H1 (1:2000, Cell Signaling), c-Myc (1:1000, Abcam), BIM (1:1000, Cell Signaling), vinculin (1:10000, Sigma); or with fluorescence as for Poly/Mono-ADP Ribose (1:1000, Cell Signaling), Poly(ADP-Ribose) Polymerase-1 antibody (1:1000, BIO-RAD), Phospho-p44/42 MAPK (Erk1/2) (Thr202/Tyr204) (1:1000, Cell Signaling), Anti-ERK (pan ERK) (1:2000, BD). Signal quantification was performed using Image Lab software, with normalization to vinculin or tubulin as appropriate. See "Reporting summary" for antibody details.

Flow cytometry

Cells were dissociated with Accutase and resuspended in 0.1% BSA (Sigma) in PBS. For NC lineage markers, cells were incubated for 30 min on ice with unconjugated p75 primary antibody (Abcam, 1:1000) and detected with Alexa Fluor 647-conjugated secondary antibodies, following incubation for 30 min on ice with unconjugated primary antibody Hnk1 (Abcam, 1:1000) and detected with Alexa Fluor 488-conjugated secondary antibodies. For MSC markers, cells were incubated with conjugated APC-CD73 (BD Pharmigen, 1:80), PE-CD13 (BD Pharmigen, 1:10) and PE-CD44 (BD Pharmigen, 1:10) for 15 min. Cells were analyzed by flow cytometry using BD FASCCanto II and analyzed using BD FACSDiva 6.2 software. See "Reporting summary" for antibody details.

Immunocytochemistry

Cells and NC spheroids were fixed in 4% paraformaldehyde (PFA) (Chem Cruz) in PBS for 15 min (cells) and 30 min (spheroids), permeabilized with 0.1%Triton X-100 in PBS for 10 min, blocked in 10% FBS in PBS for 15 min, and incubated with primary antibodies: p14ARF (1:250, Abcam), p16INKa, (1:100, Abcam) OCT3/4 (1:200, Stem Cell Technologies), TFAP2 (1:50, Thermo Scientific), SOX10 (1:400, Abcam), SOX9 (1:100, Abcam), S100B (1:1000, DAKO), p75 (1:100, Abcam) and H3K27me3 (1:2000, Cell Signaling technology), overnight at 4 °C. Secondary antibodies were Alexa Fluor 488 and Alexa Fluor 568 (Thermo Fisher Scientific). See "Reporting summary" for antibody details. Fluorescent and phase contrast images from cells and spheroids were captured using the DMI 6000B microscope (Leica) and LAS X software (Leica).

Quantitative high-throughput screen (qHTS)

A targeted chemical screen was performed using the NCATS Pharmacologically Active Chemical Toolbox (NPACT) Epigenetics qHTS Library containing 339 small molecules (Supplementary Data 7) in 3D spheroid cultures of NC-derived cells (1KO, 2KO, 3KO, and 3KO+ lines) and control fibroblast spheroids. Compounds were prepared as DMSO solutions and pre-plated in 1536-well source plates at threefold serial dilution. At 24 h post-seeding, compounds were transferred to spheroid assay plates using a 384-pin tool dispenser, and cells were incubated with compounds for 48 h at 37 °C in a humidified 5% CO_2 incubator. Cell viability was assessed using the CellTiter-Glo 3D Cell Viability Assay (Promega) following the manufacturer's instructions.

Curve response class (CRC)

Compound activity was evaluated according to the curve response class (CRC). Normalized data were fitted to four-parameter dose-response models using a custom grid-based algorithm, which assigned a CRC score to each compound's dose-response profile[60]. CRC values of −1.1, −1.2, and −2.1 were classified as high-confidence hits; values of −1.3, −1.4, −2.2, −2.3, −2.4, and −3 were considered inconclusive; whereas positive CRC values were interpreted as indicating inactive compounds[26].

Cell viability assay

Cell viability was assessed by the CellTiter-Glo® 3D Cell Viability Assay (Promega) using the manufacturer's instructions. Luminescence was recorded using the PHERAstar FSX plate reader (BMG LABTECH).

To assess cell viability and morphological changes at 48 h post-treatment in the HTS, a Live/dead staining assay was performed. A 2X staining solution was prepared by mixing DMEM/F12 (1:1) basal medium supplemented with Hoechst 33342 (1:1000; Thermo Fisher Scientific), propidium iodide (1:500; Thermo Fisher Scientific), and Calcein-AM (1:1000; Thermo Fisher Scientific). This solution was added to each well containing treated spheroids at a 1:1 volume ratio. Spheroids were incubated for 30 min at 37 °C. Following incubation,

10X confocal images were acquired using an Opera Phenix™ High-Content Screening System (PerkinElmer).

Compound combination matrix screening

Forty-eight candidate compounds from the second single agent were evaluated in combination with Selumetinib and Ribociclib in 3KO NC spheroids ($n = 1$ experiment). The 13 most promising candidates in combination with Selumetinib were selected for further validation in 3KO NC spheroids ($n = 3$ independent experiments). To assess potential off-target cytotoxicity, these 13 combinations were also tested in control fibroblast (GM00622) 3D spheroids ($n = 1$ experiment).

For matrix screening, cells were seeded into 384-well ULA round-bottom plates with 30 μL medium per well. After 24 h post-seeding, two compounds (120 nL each) were acoustically dispensed using the Echo 655 Liquid Handling System (Beckman Coulter) into one well with spheroids, in a threefold dilution of 6 × 6 blocks of dose-response matrices. Spheroids were treated with compound combinations for 48 h, after which cell viability was assessed using the CellTiter-Glo 3D Cell Viability Assay (Promega).

In vitro validation in additional 3KO NC cell lines and MPNST cell lines

384-well plates were pre-spotted at NCATS with candidate compounds at the following starting concentrations: PARP inhibitor Olaparib (20 μM) and Talazoparib (1 μM); HDAC inhibitors Entinostat (10 μM), Belinostat (10 μM), and ACY-1215 (20 μM); and BET inhibitors I-BET151 (10 μM), GSK1324726A (2 μM), Alobresib (2 μM), and CPI-0610 (20 μM). Each compound was pre-spotted as 8-point, 1:2 serial dilution, alone or in combination with Selumetinib at 20 μM, 5 μM, or 1.25 μM ($n = 2$). 3KO cell lines (3KO_H8, 3KO_C6, and 3KO_D8) and control fibroblasts were cultured as spheroids. MPNST cell lines (sNF96.2, ST88-14, and NMS-2) were cultured in 2D. Compounds were manually resuspended and pipetted (10 μL/well) in the 384-well plates. For 3D and 2D cultures, viability was assessed using the CellTiter-Glo® 3D Cell Viability Assay (Promega) and the CellTiter-Glo Luminescent Cell Viability Assay (Promega), respectively, following the manufacturer's instructions. Luminescence was recorded using the GloMax Explorer plate reader (Promega). Synergy was determined using CompuSyn software (RRID: SCR_022931), based on Chou–Talalay calculations[61].

Drugs for in vivo study and maximum tolerated dose test

Drugs for in vivo experiments were purchased from MedChemExpress: Olaparib (Cat. #HY-10162), Selumetinib (Cat. #HY-50706), I-BET151 (Cat. #HY-13235), and Ribociclib (Cat. #HY-15777). We adjusted the dosages and the administration schemes for Olaparib and combinations, using athymic nude 6-week-old male and female mice, in which no tumor was engrafted. Three mice were used for each triple combination condition (Olaparib + Selumetinib + Ribociclib; Olaparib + Selumetinib + I-BET151). The doses of Selumetinib, Ribociclib, and I-BET151 were selected based on previous studies[31]. Mice were treated for 3 weeks, and body weight was measured daily to analyze potential toxicity. The optimal doses of each compound, at which no toxicity was observed, were determined to be: Olaparib 40 mg/kg, Selumetinib 45 mg/kg, I-BET151 22 mg/kg, and Ribociclib 85 mg/kg.

In vivo drug testing on the MPNST PDOX model

The NF1-18B PDOX model established in Conxi Lazaro's Lab was used[31,33]. Tumors were expanded in 5-week-old athymic nude mice. When tumors reached 1000–1500 mm^3, they were grafted into the sciatic nerve of new 5-week-old mice. Each group consisted of 5 to 8 mice. Once tumors reached 300 to 500 mm^3, mice were randomized into treatment groups and treated for 3 weeks. If the tumor volume exceeded the permissible limit (1.5 cm in diameter), mice were sacrificed. In the absence of observed toxicity, doses of several compounds were escalated after the first 2 weeks, resulting in the following regimen: Olaparib 40 mg/kg orally once daily for the first 2 weeks, then 45 mg/kg once daily; Selumetinib 45 mg/kg orally once daily for the first 2 weeks, then 55 mg/kg once daily; I-BET151 22 mg/kg intraperitoneally 3 days per week; and Ribociclib 85 mg/kg orally once daily. Mice were sacrificed 4 to 5 h after the last dose, and tumors were removed. Liver, kidney, lung, and heart tissues were also collected and analyzed by hematoxylin and eosin (H&E) and Masson's trichrome staining for toxicity assessment. Tumors were measured using a caliper twice a week, and the volume was calculated using the formula $v = (w^2L/2)$, in which L is the longest diameter and w is the width. Statistical analyses used the Mann–Whitney test, with a significance level of 0.05.

Immunohistochemistry

Immunohistochemical staining was performed on FFPE sections following deparaffinization and rehydration using an automated platform (Benchmark Ultra, Ventana). Slides underwent heat-mediated antigen retrieval (CC1 buffer), incubation with prediluted primary antibodies (SOX10, S100, Ki67), and detection using the UltraView DAB system. For H3K27me3 and vimentin, sections were treated with 3% H_2O_2, subjected to antigen retrieval in citrate buffer (pH 6), and blocked with goat serum prior to overnight incubation with primary antibodies (1:200, 4 °C), followed by HRP-conjugated secondary antibody and DAB detection. For fluorescent immunohistochemistry, sections were rehydrated, subjected to antigen retrieval, permeabilized (Triton X-100), and blocked before incubation with primary antibodies against S100B (1:1000) and Ku80 (1:200) overnight at 4 °C. Alexa Fluor–conjugated secondary antibodies were applied, nuclei were stained with DAPI, and images were acquired by light (Nikon Eclipse 80i vertical microscope) or fluorescence microscopy (DMI 6000B microscope (Leica)).

Senescence assay

Cells were cultured until they reached 70% confluency, and senescent cells were stained using the Senescence detection kit (Sigma CS0030) following the manufacturer's instructions. Phase contrast images were captured using the DMI 6000B microscope (Leica) and LAS X software (Leica).

Ploidy and proliferation assay

For the ploidy assay, 1×10^6 cells were fixed with 70% cold ethanol overnight at −20 °C. Cells were incubated 30 min at 37 °C with 50 μg/mL propidium iodide (PI) in PBS-FBS 1% with 100 μg/mL RNase and analyzed by flow cytometry using BD FACSCanto II and BD FACSDiva 6.2 software. For the proliferation assay, cells were treated with 20 μM EdU for 1 h, fixed, permeabilized, and click labeled with Alexa Fluor 488 using Click-iT Plus EdU Flow Cytometry Assay Kits (Thermo Fisher) according to manufacturer instructions. Cells were also stained with DAPI to detect DNA content. Data was collected and analyzed using BD FASCCanto II and BD FACSDiva 6.2 software.

Lentiviral vectors and transduction

A tetracycline-inducible system was generated by sequential transduction with pLV-EF1A>Tet3G(ns):T2A:Neo and pLV-TRE3G vectors encoding either p16 (CDKN2A, NM_000077.5; IRES–mCherry) or p14 (CDKN2A, NM_058195.4; IRES–EGFP) (VectorBuilder).

Lentivirus was produced in HEK293T cells by $CaCl_2$-mediated co-transfection with psPAX2 (Addgene #12260) and pCMV-VSV-G (Addgene #8454). Viral supernatants were collected 72 h post-transfection and filtered (0.45 μm). Target cells were transduced in the presence of polybrene (8ug/mL) for 6 h and selected after 48 h with G418 (150 μg/mL), puromycin (0.2–0.4 μg/mL), or hygromycin (50 μg/mL).

For enrichment, cells were induced with doxycycline (1 µg/mL, Sigma) for 24 h and GFP$^+$ or mCherry$^+$ populations were sorted. Sorted cells were maintained without doxycycline. For induction assays, 2.5 × 10^5 cells per well were seeded in 12-well plates and treated with doxycycline (1 µg/mL) the next day. Reporter expression was assessed at 24 h, 5 days, and 8 days by flow cytometry.

Pemetrexed treatment

1KO and 2KO NC cell lines (1750 cells/well) and control fibroblasts (750 cells/well) were seeded into 384-well plates (Greiner). 24 h later, Pemetrexed (LY231514; MedChemExpress) was added in triplicate at seven concentrations using a 1:3 serial dilution starting from 30 µM. After 96 h of treatment, cell viability was measured using the CellTiter-Glo Luminescent Cell Viability Assay (Promega), and luminescence was quantified with a GloMax Explorer plate reader (Promega).

RNA-seq and analysis

Total RNA was extracted from cells using the 16 LEV simplyRNA Purification Kit (Promega) in the Maxwell 16 Instrument (Promega) following the manufacturer's instructions. Libraries were prepared at BGI (Shenzhen, China) and sequenced following DNBseq standard protocols. Raw sequencing data were quality controlled, and transcript abundances were computed with Salmon v1.8.0 (RRID:SCR_017036)[61] using UCSC refMrna and hg38 genome. Counts matrix was imported into R (R v4.3.0 Bioconductor v3.17) and summarized to the gene level using tximport (RRID:SCR_016752), keeping only genes with five or more counts in two or more samples. Differential expression analysis was performed using DESeq2 (RRID:SCR_015687)[62] with the Wald test and apeglm (RRID:SCR_015687) heatmaps were plotted with the pheatmap (RRID:SCR_016418) R package and the clusterProfiler (RRID:SCR_016884)[63] R package was used for enrichment analysis. Genes with an adjusted p-value < 0.05 were considered differentially expressed.

MPNST cell lines and PNF-derived Schwann cells RNAseq data

In this study, we used the RNA-seq data of five NF1-associated MPNST cell lines[36]: S462 (RRID:CVCL_1Y70), ST88-14 (RRID:CVCL_8916), F90-8 (RRID:CVCL_1B47), sNF96.2 (RRID:CVCL_K281) and NMS-2 (RRID:CVCL_4662). This MPNST cell line contains the most frequently inactivated tumor suppressor genes (TSGs): *NF1*, *CDKN2A* and PRC2.

In this study, we used the RNA-seq data of 3 PNF-derived SC lines[21].

ATACseq

ATACseq was performed at Diagenode (Ougrée, Belgium) from cryopreserved cells. In brief, ATAC-seq reads were mapped to the GRCh38 human reference genome using BWA-MEM[62] and deduplicated using Picard MarkDuplicates. We then called peaks with macs2[63] with standard parameters and used deeptools bamCoverage to generate bigwig files for plotting. For differential accessibility, we called consensus peaks with macs2, converted the narrowPeak files into SAF with awk and used featureCounts to create a counts table. Consensus peak counts were imported into R. edgeR[64] was used for normalization and differential analysis between genotypes (1KO and 2KO vs 3KO). Peaks were assigned to genes, and a score was calculated for each peak based on p-value, log FC and logCPM. The peak with the greatest score was selected to represent each gene in volcano plots and in plots correlating accessibility and expression. Functional enrichment was performed on GO terms with clusterProfiler[65] with genes with a p-value below 0.05 and a log fold change over ±1 independently for differentially closed and differentially open genes.

DNA methylation

DNA methylation was produced at Diagenode (Ougrée, Belgium). In short, DNA profiles were generated using the Infinium MethylationEPIC (850k) BeadChip array (Illumina, San Diego, USA) according to the manufacturer's instructions. The data was processed, normalized and filtered using minfi Bioconductor package[66]. We then represent the distribution of the samples according its processed beta values using a PCA.

Expression, methylation and accessibility intersection

The intersection of the expression, methylation, and accessibility data was based on the differential analysis performed for each technology. For expression, any gene with an adjusted p-value < 0.05 in the 2KO vs 3KO comparison was included. For ATAC-seq, any gene with a peak with a p-value < 0.05 in the 1KO and 2KO vs 3KO comparison was included. For methylation, any gene annotated in a CpG with an adjusted p-value < 0.05 in the 2KO vs 3KO comparison was included. Gene list intersection and Venn diagram creation were performed with the ggVennDiagram R package.

Plexiform neurofibromas (PNFs), ANNUBPS, MPNSTs and nerve samples for single-cell analysis

Human samples were obtained from individuals diagnosed with NF1 according to established clinical criteria[67], alongside non-NF1 control donors, following informed consent and approval by the institutional ethics committee. Tissue specimens, including tumors and peripheral nerve samples, were collected after surgery and transferred in supplemented DMEM containing 10% FBS, 2 mM GlutaMAX, and antibiotics. Upon arrival, samples were mechanically dissociated into ~1 mm fragments and cryopreserved in 10% FBS with 90% dimethyl sulfoxide until further processing.

Single-cell RNA-Seq and analysis

scRNA-seq analysis was performed at CNAG (Barcelona, Spain). Cryopreserved samples (4 nerves, 5 PNFs, 4 ANNUBPS and 3 MPNSTs) were thawed and digested with 160 U/mL Collagenase Type 1 (Worthington, Lakewood, NJ) and 0.8 U/mL Dispase (Worthington, Lakewood, NJ) for 16 h at 37 °C 5% CO_2. For PNFs, ANNUBPS and MPNSTs, the Dead Cell Removal MicroBeads kit (Miltenyi Biotec) was used to eliminate dead cells. For nerve samples, the Myelin Removal kit (Miltenyi Biotec) was used to eliminate myelin, and all procedures from this point were conducted at 4 °C. Cells were then resuspended in DMEM + 10% FBS (Gibco) + 1x GlutaMAX (Gibco), filtered with a 40 mm filter, and cell viability was calculated with the TC20TM Automated Cell Counter (Bio-Rad). scRNA-seq libraries were built following standard protocols and sequenced using an Illumina platform. FASTQ files were processed with cellranger-arc version 2.0.1 (10X Genomics) using the 2020-A-2.0.0 reference based on GRCh38 and Ensembl genes, and multiple samples were combined using the cellranger-arc aggr command with the option "–normalize=depth". Merged UMIs per gene per cell matrix were then loaded into R. We performed quality check, filtering (low library size, high mitochondrial content, low number of features) and normalization using scater[68]. We removed highly stressed cells from one sample (scYoga) and doublets (scDblFinder)[69]. Data was batch corrected with fastMNN from package batchelor[70]. Cell types were assigned with SingleR[71] based on the HumanPrimaryCellAtlas reference[72]. For the graphical representation, we performed a dimensionality reduction step with PCA and T-distributed Stochastic Neighbor Embedding (TSNE).

WGS

Genomic DNA from cells was extracted using Promega Maxwell 16 system following the manufacturer's instructions (Promega) and sequenced at BGI (Shenzen, China) following the DNBseq protocols in a BGISEQ-500 instrument. Paired-end raw data (2 × 150bp) was mapped to the GRCh38 reference genome using BWA-MEM[62] and copy-number variation was called with CNVkit[73] with WGS settings and using a panel of normals. We used Strelka2 in germline mode to call small

variants and the CopyNumberPlots R/Bioconductor package (10.18129/B9.bioc.CopyNumberPlots) to compute a pseudo-BAF and LRR and combined it with karyoploteR[74] for plotting.

Statistical analysis

Statistical analyses were performed using GraphPad Prism 10 software. Data are shown as mean ± standard deviation (SD). Pairwise comparisons between groups in in vitro experiments were carried out using a two-tailed unpaired Student's *t* test. For all analyses, the cutoff was set as $^{*}p < 0.05$; $^{***}p < 0.001$; $^{****}p < 0.0001$. In vitro compound testing data are reported as mean ± standard deviation (SD), and the Z′ (Z-prime) factor was used to determine the quality and robustness of the cellular model for drug screening assays. For in vivo experiments, 5 to 8 animals per group were used, with 80% power to detect a minimum of 50% tumor differences ($p = 0.05$). Statistical analyses used the Mann–Whitney test, with a significance level at $^{*}p < 0.05$. Source data and exact *p*-values are provided as a Source Data file.

Data visualization

ATAC-seq coverage plots were created from bigwig files with karyoploteR[74]. Heatmaps were plotted with ComplexHeatmap[75]. Boxplots of neurogenesis genes were plotted using R after standardizing the expression data to mean = 0 and sd = 1. Schemes and diagrams were created with Biorender. Low-throughput molecular data were analyzed and plotted with GraphPad Prism (version 7.00).

Reporting summary

Further information on research design is available in the Nature Portfolio Reporting Summary linked to this article.

Data availability

All data have been deposited on the European Genome-Phenome Archive (EGA) (https://ega-archive.org/). Single-cell transcriptome data can be found under accession EGAD50000002508 and all other data under accession EGAD50000002533. Source data are provided with this paper.

References

1. Lafemina, J. et al. Oncologic outcomes of sporadic, neurofibromatosis-associated, and radiation-induced malignant peripheral nerve sheath tumors. *Ann. Surg. Oncol.* **20**, 66 (2012).
2. Evans, D. G. R. et al. Malignant peripheral nerve sheath tumours in neurofibromatosis. *J. Med. Genet.* **39**, 311–314 (2002).
3. Uusitalo, E. et al. Distinctive cancer associations in patients with neurofibromatosis type 1. *J. Clin. Oncol.* **34**, 1978–1986 (2016).
4. Porter, D. E. et al. Survival in malignant peripheral nerve sheath tumours: a comparison between sporadic and neurofibromatosis type 1-associated tumours. *Sarcoma* **2009**, 756395 (2009).
5. Moretti, V. M., Crawford, E. A., Staddon, A. P., Lackman, R. D. & Ogilvie, C. M. Early outcomes for malignant peripheral nerve sheath tumor treated with chemotherapy. *Am. J. Clin. Oncol. Cancer Clin. Trials* **34**, 417–421 (2011).
6. Beert, E. et al. Atypical neurofibromas in neurofibromatosis type 1 are premalignant tumors. *Genes Chromosomes Cancer* **50**, 1021–1032 (2011).
7. Carrió, M. et al. Analysis of intratumor heterogeneity in neurofibromatosis type 1 plexiform neurofibromas and neurofibromas with atypical features: correlating histological and genomic findings. *Hum. Mutat.* **39**, 1112–1125 (2018).
8. Lee, W. et al. PRC2 is recurrently inactivated through EED or SUZ12 loss in malignant peripheral nerve sheath tumors. *Nat. Genet.* **46**, 1227–1232 (2014).
9. Buchstaller, J., Clapp, D. W., Parada, L. F. & Zhu, Y. *Cell of Origin and the Contribution of Microenvironment in NF1 Tumorigenesis and Therapeutic Implications*. *Neurofibromatosis Type 1: Molecular and Cellular Biology* (Springer, 2012).
10. Miettinen, M. M. et al. Histopathologic evaluation of atypical neurofibromatous tumors and their transformation into malignant peripheral nerve sheath tumor in patients with neurofibromatosis 1—a consensus overview. *Hum. Pathol.* **67**, 1–10 (2017).
11. Higham, C. S. et al. The characteristics of 76 atypical neurofibromas as precursors to neurofibromatosis 1 associated malignant peripheral nerve sheath tumors. *Neuro-Oncol.* **20**, 818–825 (2018).
12. Comet, I., Riising, E. M., Leblanc, B. & Helin, K. Maintaining cell identity: PRC2-mediated regulation of transcription and cancer. *Nat. Rev. Cancer* **16**, 803–810 (2016).
13. De Raedt, T. et al. PRC2 loss amplifies Ras-driven transcription and confers sensitivity to BRD4-based therapies. *Nature* **514**, 247–251 (2014).
14. Verdijk, R. M. et al. TP53 mutation analysis of malignant peripheral nerve sheath tumors. *J. Neuropathol. Exp. Neurol.* **69**, 16–26 (2010).
15. Radomska, K. J. et al. Glial-to-mesenchymal transition of tumor Schwann cells drives the genetic burden in MPNSTs from neurofibromatosis type 1 mouse model. *Sci. Adv.* **11**, eadt9210 (2025).
16. Rhodes, S. D. et al. *Cdkn2a* (*Arf*) loss drives NF1-associated atypical neurofibroma and malignant transformation. *Hum. Mol. Genet.* **28**, 2752–2762 (2019).
17. Chaney, K. E. et al. *Cdkn2a* loss in a model of neurofibroma demonstrates stepwise tumor progression to atypical neurofibroma and MPNST. *Cancer Res.* **80**, 4720–4730 (2021).
18. Ferrer, M. et al. Pharmacological and genomic profiling of neurofibromatosis type 1 plexiform neurofibroma-derived Schwann cells. *Sci. Data* **5**, 1–12 (2018).
19. Williams, K. B. et al. Pharmacogenomic synthetic lethal screens reveal hidden vulnerabilities and new therapeutic approaches for treatment of NF1-associated tumors. *Mol. Cancer Ther.* **25**, 230–243 (2026).
20. Fernández-Rodríguez, J. et al. A high-throughput screening platform identifies novel combination treatments for malignant peripheral nerve sheath tumors. *Mol. Cancer Ther.* **21**, 1246–1258 (2022).
21. Mazuelas, H. et al. Modeling iPSC-derived human neurofibroma-like tumors in mice uncovers the heterogeneity of Schwann cells within plexiform neurofibromas. *Cell Rep.* **38**, 110385 (2022).
22. Mazuelas, H. et al. Generation of human iPSC-derived neurofibromaspheres for in vitro and in vivo uses. *STAR Protoc.* **4**, 102198 (2023).
23. Benfatto, S. et al. Uncovering cancer vulnerabilities by machine learning prediction of synthetic lethality. *Mol. Cancer* **20**, 1–22 (2021).
24. Magallón-Lorenz, M. et al. Chromosomal translocations inactivating CDKN2A support a single path for malignant peripheral nerve sheath tumor initiation. *Hum. Genet.* **140**, 1241–1252 (2021).
25. Carrió, M. et al. Reprogramming captures the genetic and tumorigenic properties of neurofibromatosis type 1 plexiform neurofibromas. *Stem Cell Rep.* **12**, 639 (2019).
26. Huang, R. A quantitative high-throughput screening data analysis pipeline for activity profiling. *Methods Mol. Biol.* **2474**, 133–145 (2022).
27. Butler, E. et al. Functional imaging of RAS pathway targeting in malignant peripheral nerve sheath tumor cells and xenografts. *Pediatr. Blood Cancer* **67**, e28639 (2020).
28. Ahsan, S. et al. Combinatorial therapeutic targeting of BMP2 and MEK-ERK pathways in NF1-associated malignant peripheral nerve sheath tumors. *Oncotarget* **7**, 57171–57185 (2016).
29. Zamora, P. O. et al. Drug responses in plexiform neurofibroma type I (PNF1) cell lines using high-throughput data and combined effectiveness and potency. *Cancers* **15**, 5811 (2023).

30. Wang, J. et al. CDK4/6 inhibition enhances SHP2 inhibitor efficacy and is dependent upon RB function in malignant peripheral nerve sheath tumors. *Sci Adv*. **9**, eadg8876 (2023).
31. Ortega-Bertran, S. et al. Triple combination of MEK, BET, and CDK inhibitors significantly reduces human malignant peripheral nerve sheath tumors in mouse models. *Clin. Cancer Res.* **31**, 907–920 (2025).
32. Kohlmeyer, J. L. et al. CDK4/6-MEK inhibition in MPNSTs causes plasma cell infiltration, sensitization to PD-L1 blockade, and tumor regression. *Clin. Cancer Res.* **29**, 3484–3497 (2023).
33. Ortega-Bertran, S. et al. New models for MPNST: establishment and comprehensive characterization of two tumor cell lines. *Cancer Cell Int.* **25**, 1–13 (2025).
34. Kanev, P. B. et al. A unified mechanism for PARP inhibitor-induced PARP1 chromatin retention at DNA damage sites in living cells. *Cell Rep.* **43**, 114234 (2024).
35. Lucas, C. H. G. et al. Consensus recommendations for an integrated diagnostic approach to peripheral nerve sheath tumors arising in the setting of neurofibromatosis type 1. *Neuro-Oncol.* **27**, 616–624 (2025).
36. Magallón-Lorenz, M. et al. Deep genomic analysis of malignant peripheral nerve sheath tumor cell lines challenges current malignant peripheral nerve sheath tumor diagnosis. *iScience* **26**, 106096 (2023).
37. Lee, T. I. et al. Control of developmental regulators by Polycomb in human embryonic stem. *Cell* **125**, 301–313 (2006).
38. De Raedt, T. et al. Somatic loss of wild type NF1 allele in neurofibromas: comparison of NF1 microdeletion and non-microdeletion patients. *Genes Chromosomes Cancer* **45**, 893–904 (2006).
39. Bracken, A. P. et al. The Polycomb group proteins bind throughout the INK4A-ARF locus and are disassociated in senescent cells. *Genes Dev.* **21**, 525 (2007).
40. Gomez-Sanchez, J. A. et al. Epigenetic induction of the Ink4a/Arf locus prevents Schwann cell overproliferation during nerve regeneration and after tumorigenic challenge. *Brain* **136**, 2262–2278 (2013).
41. Wu, L. M. N. et al. Single-cell multiomics identifies clinically relevant mesenchymal stem-like cells and key regulators for MPNST malignancy. *Sci. Adv.* **8**, eabo5442 (2022).
42. Kochat, V. et al. Enhancer reprogramming in PRC2-deficient malignant peripheral nerve sheath tumors induces a targetable de-differentiated state. *Acta Neuropathol.* **142**, 565–590 (2021).
43. Zhang, X. et al. Single-cell sequencing reveals activation of core transcription factors in PRC2-deficient malignant peripheral nerve sheath tumor. *Cell Rep.* **40**, 111363 (2022).
44. Vasudevan, H. N. et al. Functional interactions between neurofibromatosis tumor suppressors underlie Schwann cell tumor de-differentiation and treatment resistance. *Nat. Commun.* **15**, 477 (2024).
45. Britsch, S. et al. The transcription factor Sox10 is a key regulator of peripheral glial development. *Genes Dev.* **15**, 66 (2001).
46. Miller, S. J. et al. Large-scale molecular comparison of human Schwann cells to malignant peripheral nerve sheath tumor cell lines and tissues. *Cancer Res.* **66**, 2584–2591 (2006).
47. Miller, S. J. et al. Integrative genomic analyses of neurofibromatosis tumours identify SOX9 as a biomarker and survival gene. *EMBO Mol. Med.* **1**, 236–248 (2009).
48. Dietrich, N. et al. REST–mediated recruitment of Polycomb repressor complexes in mammalian cells. *PLoS Genet.* **8**, e1002494 (2012).
49. Lopez, G. et al. Autophagic survival in resistance to histone deacetylase inhibitors: novel strategies to treat malignant peripheral nerve sheath tumors. *Cancer Res.* **71**, 185–196 (2011).
50. Patel, A. V. et al. Ras-driven transcriptome analysis identifies aurora kinase A as a potential malignant peripheral nerve sheath tumor therapeutic target. *Clin. Cancer Res.* **18**, 5020–5030 (2012).
51. Patel, A. J. et al. BET bromodomain inhibition triggers apoptosis of NF1-associated malignant peripheral nerve sheath tumors through bim induction. *Cell Rep.* **6**, 81–92 (2014).
52. Sun, C. et al. Rational combination therapy with PARP and MEK inhibitors capitalizes on therapeutic liabilities in RAS mutant cancers. *Sci. Transl. Med.* **9**, eaal5148 (2017).
53. Xiao, Q. et al. Combined MEK and PARP inhibition enhances radiation response in rectal cancer. *Cell Rep. Med.* **6**, 102284 (2025).
54. Li, S. et al. Pan-cancer analysis reveals synergistic effects of CDK4/6i and PARPi combination treatment in RB-proficient and RB-deficient breast cancer cells. *Cell Death Dis.* **11**, 1–16 (2020).
55. Yang, L. et al. Repression of BET activity sensitizes homologous recombination-proficient cancers to PARP inhibition. *Sci. Transl. Med.* **9**, eaal1645 (2017).
56. Aftimos, P. G. et al. A phase 1b/2 study of the BET inhibitor ZEN-3694 in combination with talazoparib for treatment of patients with TNBC without gBRCA1/2 mutations. *J. Clin. Oncol.* **40**, 1023–1023 (2022).
57. Kivlin, C. M. et al. Poly (ADP) ribose polymerase inhibition: a potential treatment of malignant peripheral nerve sheath tumor. *Cancer Biol. Ther.* **17**, 129–138 (2016).
58. Larsson, A. T. et al. Ex vivo to in vivo model of malignant peripheral nerve sheath tumors for precision oncology. *Neuro-Oncol.* **25**, 2044–2057 (2023).
59. Menendez, L. et al. Directed differentiation of human pluripotent cells to neural crest stem cells. *Nat. Protoc.* **8**, 203–212 (2013).
60. Wang, Y., Jadhav, A., Southal, N., Huang, R. & Nguyen, D. T. A grid algorithm for high throughput fitting of dose-response curve data. *AACE Clin. Case Rep.* **7**, 1 (2021).
61. Chou, T. C. Drug combination studies and their synergy quantification using the Chou-Talalay method. *Cancer Res.* **70**, 440–446 (2010).
62. Li, H. Aligning sequence reads, clone sequences and assembly contigs with BWA-MEM. Preprint at *arXiv* https://arxiv.org/pdf/1303.3997 (2013).
63. Zhang, Y. et al. Model-based analysis of ChIP-Seq (MACS). *Genome Biol.* **9**, 1–9 (2008).
64. Robinson, M. D., McCarthy, D. J. & Smyth, G. K. edgeR: a Bioconductor package for differential expression analysis of digital gene expression data. *Bioinformatics* **26**, 139–140 (2010).
65. Yu, G., Wang, L. G., Han, Y. & He, Q. Y. ClusterProfiler: an R package for comparing biological themes among gene clusters. *OMICS* **16**, 284–287 (2012).
66. Aryee, M. J. et al. Minfi: a flexible and comprehensive Bioconductor package for the analysis of Infinium DNA methylation microarrays. *Bioinformatics* **30**, 1363–1369 (2014).
67. DeBella, K., Szudek, J. & Friedman, J. M. Use of the National Institutes of Health criteria for diagnosis of neurofibromatosis 1 in children. *Pediatrics* **105**, 608–614 (2000).
68. McCarthy, D. J., Campbell, K. R., Lun, A. T. L. & Wills, Q. F. Scater: pre-processing, quality control, normalization and visualization of single-cell RNA-seq data in R. *Bioinformatics* **33**, 1179–1186 (2017).
69. Germain, P. L., Robinson, M. D., Lun, A., Garcia Meixide, C. & Macnair, W. Doublet identification in single-cell sequencing data using scDblFinder. *F1000Res.* **10**, 979 (2022).
70. Haghverdi, L., Lun, A. T. L., Morgan, M. D. & Marioni, J. C. Batch effects in single-cell RNA-sequencing data are corrected by matching mutual nearest neighbors. *Nat. Biotechnol.* **36**, 421–427 (2018).
71. Mabbott, N. A., Baillie, J. K., Brown, H., Freeman, T. C. & Hume, D. A. An expression atlas of human primary cells: inference of gene

function from coexpression networks. *BMC Genomics* **14**, 1–13 (2013).
72. Aran, D. et al. Reference-based analysis of lung single-cell sequencing reveals a transitional profibrotic macrophage. *Nat. Immunol.* **20**, 163–172 (2019).
73. Talevich, E., Shain, A. H., Botton, T. & Bastian, B. C. CNVkit: genome-wide copy number detection and visualization from targeted DNA sequencing. *PLoS Comput. Biol.* **12**, e1004873 (2016).
74. Gel, B. & Serra, E. karyoploteR: an R/Bioconductor package to plot customizable genomes displaying arbitrary data. *Bioinformatics* **33**, 3088–3090 (2017).
75. Gu, Z., Eils, R. & Schlesner, M. Complex heatmaps reveal patterns and correlations in multidimensional genomic data. *Bioinformatics* **32**, 2847–2849 (2016).

Acknowledgements

We thank the IGTP core facilities and their staff for their contribution and technical support: Translational Genomics Core Facility; Cryobiology, High Performance Computing; Flow Cytometry (Gerard Requena, Joan Puñet Ortiz and Marco A. Fernández); IGTP-Hospital Universitari Germans Trias i Pujol (HUGTP) Biobank Facility (Laia Pérez-Roca, Christel Kisser Pioch, Reyes Rodríguez and Lidia Nieto) and Pathology Department (Dr. Pedro Luis González). We thank the Barcelona Stem Cell Bank, Regenerative Medicine Program, IDIBELL, Barcelona, for providing the control iPSC line. We also thank the Compound Management team and the Bioprinting Lab at NCATS. We also thank the Endocrine Tumor research group led by Dr. Mireia Jordà (IGTP), and particularly Jennifer Marcos and Anna Rueda, for kindly providing lentiviral plasmids and assisting us with the transduction procedures. We are also grateful to the Fundación Proyecto Neurofibromatosis, the Asociación de Afectados de Neurofibromatosis (AANF), and the Catalan Neurofibromatosis Association (ACNefi) for their constant support. Finally, we like to thank the constant support of the Neurofibromatosis Therapeutic Acceleration Program (NTAP) in the development of iPSC-derived NF1 models.

Author contributions

Conceptualization: E.S., M.C., I.U.-A., M.M.-L., and B.G.; methodology: I.U.-A., M.C., J.F.-R., J.Z., and E.L.; software and formal analysis: M.M.-L. and B.G.; investigation: I.U.-A., J.F.-R., M.M.-L., J.Z., E.L., B.G., H.M., E.C.-B., J.F.-C., S.O.-B., K.M.W., C.M., K.R., C.R., M.C., and E.S.; resources: I.B., H.S., C.L., M.F., and E.S.; writing—original draft: I.U.-A., M.C., and E.S.; writing—review & editing: M.M.-L., B.G., I.U.-A., J.Z., J.F.-C., M.F., M.C., and E.S.; visualization: I.U.-A., M.M.-L., B.G., M.C., and E.S.; supervision: B.G., M.F., M.C., and E.S.; project administration: M.C. and E.S.; funding acquisition: M.F. and E.S.

Funding

E.S. discloses main support for the research of this work from La Marató de TV3 [grant number 51/C/2019] and Children's Tumor Foundation Drug Discovery Initiative [grant number CTF-2023-05-001]. E.S. also discloses support from the Spanish Ministry of Science and Innovation, Carlos III Health Institute (ISCIII) [grant number PI20/00228, PI23/00422] Plan Estatal de I + D + I 2013–2016, co-financed by the FEDER program—a way to build Europe, Government of Catalonia and CERCA Program/Generalitat de Catalunya [grant number 2021 SGR 00967] and Fundación Proyecto Neurofibromatosis. B.G. discloses support from the Spanish Ministry of Science and Innovation, Carlos III Health Institute (ISCIII) [grant number PI20/00228, PI23/00583]. C.L. discloses support from La Marató de TV3 [grant number 51/C/2019]. The contributions of the NIH author(s) are made as part of their official duties as NIH federal employees in compliance with agency policy requirements and are considered works of the United States Government. However, the findings and conclusions presented in this paper are those of the author(s) and do not necessarily reflect the views of the NIH or the U.S. Department of Health and Human Services. E.S. also discloses that single-cell data used in this work were generated thanks to the support of the Department of Defense office of the Congressionally Directed Medical Research Programs (CDMRP) NFRP FY20 [grant number NF200051]. I.U.-A. and E.S. disclose that I.U.-A. has been supported by a PFIS fellowship from the ISCIII [grant number FI21/00063].

Competing interests

The authors declare no competing interests.

Additional information

Supplementary information The online version contains supplementary material available at https://doi.org/10.1038/s41467-026-73119-8.

Correspondence and requests for materials should be addressed to Bernat Gel, Marc Ferrer, Meritxell Carrió or Eduard Serra.

Peer review information *Nature Communications* thanks Yutaka Suzuki and the other anonymous reviewer(s) for their contribution to the peer review of this work. A peer review file is available.

Itziar Uriarte-Arrazola[1], Míriam Magallón-Lorenz[2], Juana Fernández-Rodríguez[3,4,5,6], Jiajing Zhang[7], Emily Lee[7], Sara Ortega-Bertran[3,4], Edgar Creus-Bachiller[3,4], Judit Farrés-Casas[1], Kelli M. Wilson[8], Crystal McKnight[8], Katlin Recabo[8], Ignacio Blanco[9], Héctor Salvador[10], Cleofé Romagosa[11], Conxi Lázaro[3,4,6], Helena Mazuelas[1], Bernat Gel[2,12] ✉, Marc Ferrer[7] ✉, Meritxell Carrió[1,13] ✉ & Eduard Serra[1,6,13] ✉

[1]Hereditary Cancer Group, CARE Program, Germans Trias i Pujol Research Institute (IGTP), Barcelona, Spain. [2]Translational Bioinformatics and Genomics of Cancer, CARE Program, Germans Trias i Pujol Research Institute (IGTP), Barcelona, Spain. [3]Hereditary Cancer Program, Catalan Institute of Oncology (ICO-IDIBELL), L'Hospitalet de Llobregat, Barcelona, Spain. [4]Program in Molecular Mechanisms and Experimental Therapy in Oncology (Oncobell), IDIBELL, Hospitalet de Llobregat, Barcelona, Spain. [5]Mouse Lab, SCT-IDIBELL, Hospitalet de Llobregat, Barcelona, Spain. [6]Centro de Investigación Biomédica en Red de Cáncer (CIBERONC), Madrid, Spain. [7]3D Tissue Bioprinting Laboratory, Division of Preclinical Innovation, National Center for Advancing Translational Sciences (NCATS), Rockville, MD, USA. [8]Compound Management, Division of Preclinical Innovation, National Center for Advancing Translational Sciences (NCATS), Rockville, MD, USA. [9]Clinical Genetics Department, Laboratori Clínic de la Metropolitana Nord, Hospital Universitari Germans Trias i Pujol, Barcelona, Spain. [10]Pediatric Oncology Department, Sant Joan de Déu Barcelona Children's Hospital, Barcelona, Spain. [11]Pathology Department, Hospital Universitari Vall d'Hebron, Barcelona, Spain. [12]Departament de Fonaments Clínics, Facultat de Medicina i Ciències de la Salut, Universitat de Barcelona (UB), Barcelona, Spain. [13]These authors jointly supervised this work: Meritxell Carrió, Eduard Serra. ✉e-mail: bgel@igtp.cat; marc.ferrer@nih.gov; mcarriol@igtp.cat; eserra@igtp.cat